

Falling film on an anisotropic porous medium

Sanghasri Mukhopadhyay¹, Nicolas Cellier¹, Usha R², Marx Chhay¹ and Christian Ruyer-Quil^{1,†}

¹Université Savoie Mont Blanc, CNRS, LOCIE, 73000 Chambéry, France

²Department of Mathematics, IIT Madras, Chennai, 600036 Tamil Nadu, India

(Received 17 March 2022; revised 29 June 2022; accepted 14 July 2022)

The stability and dynamics of a falling liquid film over an anisotropic porous medium are studied using a one-domain approach. Our stability analysis shows a significant departure from the effective no-slip boundary condition in the isotropic case. Anisotropy does not affect the threshold of linear instability. However, a non-trivial dual effect of anisotropy on the film stability is observed depending on the permeability of the porous medium. This dual effect results from the net balance of the enhancement of viscous diffusion at the top Brinkman sublayer and the mitigation of viscous damping in the core Darcy sublayer. Three-equation models have been derived from the lubrication theory approximation in terms of the exact mass balance and averaged momentum balances in the porous and liquid layers. In the nonlinear regime, anisotropy has a dual effect by damping capillary waves at large permeabilities and enhancing them at low permeabilities. Anisotropy also affects wave speeds and shapes, modifies travelling-wave branches of solutions, affects the development of a time-periodic wavetrain by inlet forcing and alters the noise-driven dynamics of the flow. These effects result from the mitigation of mass exchange at the liquid–porous interface and the contribution of the cross-stream permeability in the Brinkman top sublayer to the viscous diffusion.

Key words: thin films, lubrication theory

1. Introduction

Falling liquid film flows are commonly used in chemical engineering whenever pressure drops or boiling may be avoided. Classic examples are evaporators in the food industry for the concentration of heat-sensitive products (Silveira *et al.* 2015), packed-bed heat exchangers (de Wasch & Froment 1972) and reactors (Duarte, Ferretti & Lemcoff 1984), or distillation columns for the separation of components with close boiling points, in which case large-scale separation towers are required. For the latter, the configuration of choice is

[†] Email address for correspondence: christian.ruyer-quil@univ-smb.fr

a countercurrent contact between an upward gas and a downward liquid film distributed on a structured packing. The ideal design of the structured packing should limit the pressure drops and improve the mass transfer efficiency. The metal sheets constituting the packing are generally perforated to promote the distribution of the liquid and further reduce the pressure drop. For similar reasons, new wire gauze packing has been proposed by Amini *et al.* (2019).

Instabilities of the liquid film are known to enhance heat or mass transfer by promoting surface waves significantly (Frisk & Davis 1972; Yoshimura, Nosoko & Nagata 1996), and this mechanism is generally believed to play a crucial role in the efficiency of packed-bed exchangers. However, little is known about the influence of the permeability of the wire gauze or perforated sheets on the liquid film instabilities. In an attempt to better understand this effect on the film surface-wave hydrodynamics, we consider a falling liquid film flow on an anisotropic porous medium in this study. The introduction of different streamwise and cross-stream permeabilities of an otherwise homogeneous porous medium is a simplified modelling of the orientation of the perforations of metal sheets and wire orientations of gauze packings.

The onset of surface-wave instabilities in film flows on an inclined impermeable plate is well documented (see, for instance, the reviews by Chang & Demekhin (2002), Craster & Matar (2009) and Kalliadasis *et al.* (2012)). However, the hydrodynamics of a liquid film flow over a porous substrate has attracted relatively less attention.

The crucial part of studying the flow of a thin film overlying a porous substrate is the fluid–porous interface, which is heterogeneous irrespective of the homogeneity of the bulk fluid or the bulk porous medium. Several attempts to understand the characteristics of flow through this heterogeneous interface have resulted in different levels of descriptions depending on the choice of scale, different models and different sets of appropriate boundary conditions at the interface (Ochoa-Tapia & Whitaker 1995; Chandesris & Jamet 2006; Angot, Goyeau & Ochoa-Tapia 2017).

Among the various modelling approaches of the fluid–porous configuration, we chose the modelling approach initially proposed by Arquis & Caltagirone (1984), termed the one-domain approach. This methodology has been previously adopted by many researchers (Beckermann, Viskanta & Ramadhyani 1988; Gobin, Goyeau & Songbe 1998; Aguilar-Madera *et al.* 2011; Samanta, Goyeau & Ruyer-Quil 2013; Chen & Wang 2014; Valdés-Parada & Lasseux 2021) to study heat transfer, instability, transport phenomena, etc. In this approach, the entire system of the homogeneous bulk fluid and porous medium and their heterogeneous transitional inter-region has been considered as a single composite domain (continuum), where a single average momentum transport equation is valid in the entire continuum. The characteristic properties, like porosity and permeability, are taken to be continuous throughout the domain. In the interfacial region of the liquid and porous layer, permeability and porosity show a rapid but continuous spatial variation. This approach, being easy to handle numerically, is widely used for flow over a porous medium.

Beavers, Sparrow & Magnuson (1970) were the first to confirm the destabilising effect of wall permeability experimentally in a parallel-plate channel with one bounding wall as a porous medium. Keeping the flow configuration the same as in Beavers *et al.* (1970), Sparrow *et al.* (1973) performed an experiment to determine the critical Reynolds number and supported their findings numerically by analysing the two-dimensional flow using the Darcy model with the Beavers–Joseph interfacial condition. They established that the wall permeability decreased the critical Reynolds number (Chang, Chen & Straughan 2006; Hill & Straughan 2008). Tilton & Cortelezzi (2006, 2008) confirmed this result using the volume-averaged Navier–Stokes equations.

Pascal (1999) considered the stability of a thin fluid layer flowing down a permeable wall, proceeding with the formulation given by Yih (1963) for an impermeable wall. The study used the Darcy law to describe the flow in a porous medium with Beavers–Joseph slip boundary condition (Beavers & Joseph 1967) at the fluid–porous interface. The study showed that, in the case of a low superficial velocity in the porous medium, the presence of the porous medium could be modelled by an impermeable wall with a Navier slip boundary condition. In this regards, a destabilising effect of the Navier slip condition was observed, which was later confirmed by many researchers (Sadiq & Usha 2008; Samanta, Ruyer-Quil & Goyeau 2011).

Liu & Liu (2009) solved the linear stability eigenvalue problem of the two-sided coupled fluid–porous model using the Chebyshev collocation method. They considered the Darcy law as a porous-medium momentum transport model and Beavers–Joseph slip boundary condition at the interface. They claimed that, qualitatively, one- and two-sided models display similar results for moderately low permeability and substrate thickness. Camporeale, Mantelli & Manes (2013) demonstrated the interplay among the different unstable modes of instability that exist due to the presence of a deformable interface in a gravity-driven film flowing over a porous wall. The study reported the importance of inertial effects on the stability of the film at higher values of mean permeability.

The above-mentioned investigations have considered the porous medium as isotropic. However, there are several real-life scenarios, such as the ground structure of geothermal systems composed of many layers of different permeabilities, where permeability is not constant; in fact, the horizontal permeability may be 10 times as large as the vertical component. This motivated earlier studies on convection in an anisotropic porous medium (Castinel & Combarrous 1975; Epherre 1975).

Deepu *et al.* (2016) studied the hydrodynamic stability of a falling film over an almost horizontal anisotropic and inhomogeneous porous medium. They considered a generalised Darcy law to describe the flow in the porous medium coupled to the Beavers–Joseph boundary condition at the interface. They concluded that anisotropy has no visible effect on the linear stability of the surface mode. Our motivation for the present study is to determine the effect of anisotropy in the hydrodynamics of film flow over a porous medium with variable permeability sealed at its bottom by an impermeable condition.

The rest of the paper is organised as follows. Section 2 presents the governing equations for the one-domain approach. Section 3 is devoted to the linear stability of the Nusselt uniform-film solution. A new weighted-residual strategy is detailed in §4. Nonlinear travelling-wave (TW) solutions and time-dependent simulations are discussed in §§ 5 and 6. Section 7 summarises our work and presents the conclusions.

2. Governing equations

We consider a two-dimensional viscous, incompressible thin liquid film flowing under the action of gravity on a saturated inclined anisotropic porous plate of height d . The porous medium is considered to be bounded on one side by a rigid wall (see figure 1). Fundamental fluid properties, i.e. density (ρ), surface tension (σ) and kinematic viscosity (ν), are supposed to remain constant. The thickness of the entire domain, comprising the porous substrate and the liquid layer, is denoted by H . The origin of the vertical axis is chosen at the solid boundary, x refers to the coordinate in the flow direction and y to the cross-stream direction. The porous medium is uniform, with a constant porosity ε , but anisotropic, with different permeabilities κ_{xH} and κ_{yH} in the streamwise x and cross-stream y directions. The ‘one-domain’ approach considers a composite domain

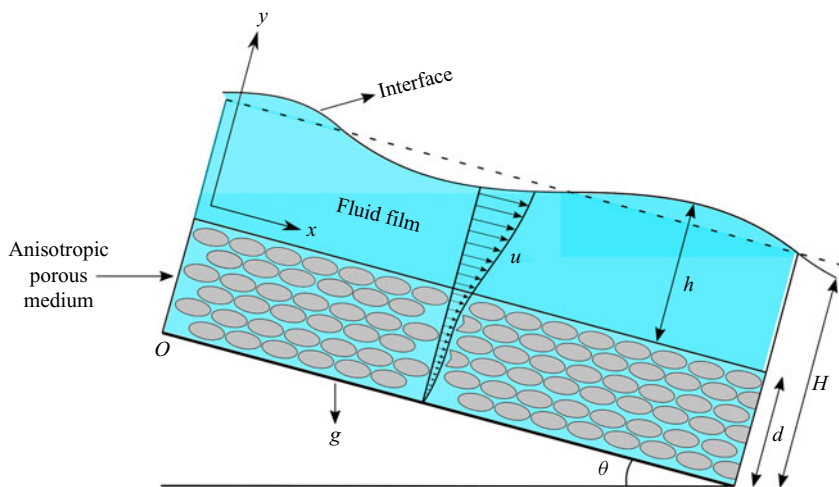


Figure 1. Schematic diagram of a falling film over an anisotropic saturated porous medium.

where the properties of the medium vary continuously from those of the porous medium to those of the liquid medium in a thin transitional region which replaces the liquid–porous interface. Material properties, such as porosity (ε) and permeability in the y direction (κ_y), show significant and continuous variations in the transitional layer from constant values ε_H and κ_{2H} in the porous medium to the values 1 and ∞ in the liquid layer. Apart from this zone, the porous medium is considered to be homogeneous.

The dimensionless governing equations for the liquid and porous medium are given by (Hirata, Goyeau & Gobin 2009)

$$u_x + v_y = 0, \quad (2.1a)$$

$$\frac{Re}{\varepsilon(y)} \left[u_t + \frac{1}{\varepsilon}(uu_x + vv_y) + uv \frac{\partial}{\partial y} \left(\frac{1}{\varepsilon} \right) \right] = -Re p_x + \frac{1}{\varepsilon}(u_{xx} + u_{yy}) - \frac{u}{\kappa_x(y)} + \frac{Re}{Fr^2}, \quad (2.1b)$$

$$\frac{Re}{\varepsilon(y)} \left[v_t + \frac{1}{\varepsilon}(uv_x + vv_y) + v^2 \frac{\partial}{\partial y} \left(\frac{1}{\varepsilon} \right) \right] = -Re p_y + \frac{1}{\varepsilon}(v_{xx} + v_{yy}) - \frac{v}{\kappa_y(y)} - \cot \theta \frac{Re}{Fr^2}. \quad (2.1c)$$

The boundary conditions are

$$\text{at } y = 0, \quad u = 0, \quad v = 0. \quad (2.1d)$$

At the free surface $y = H$ we have the conditions

$$H_t + uH_x = v, \quad (2.1e)$$

$$-4u_x H_x + (u_y + v_x)(1 - H_x^2) = 0, \quad (2.1f)$$

$$p - \frac{2}{Re(1 + H_x^2)}(H_x^2 u_x - (u_y + v_x)H_x + v_y) = -\frac{We H_{xx}}{(1 + H_x^2)^{3/2}}. \quad (2.1g)$$

The distributions of porosity, $\varepsilon(y)$, and permeabilities, $\kappa_x(y)$ and $\kappa_y(y)$, are assumed to follow hyperbolic tangent profiles, which allow one to control easily the thickness of the

transition layer of typical thickness Δ :

$$\varepsilon(y) = \frac{1 + \varepsilon_H}{2} + \frac{1 - \varepsilon_H}{2} \tanh\left[\frac{y - \delta}{\Delta}\right], \quad (2.1h)$$

$$\frac{1}{\kappa_x(y)} = \frac{1}{Da} \left(\frac{1}{2} - \frac{1}{2} \tanh\left[\frac{y - \delta}{\Delta}\right] \right), \quad \frac{1}{\kappa_y(y)} = \frac{\xi}{\kappa_x(y)}, \quad (2.1i)$$

where δ refers to the dimensionless thickness of the porous medium. In the limit $\varepsilon \rightarrow 1$, $\kappa_x, \kappa_y \rightarrow \infty$, equations (2.1b) and (2.1c) reduce to the classical momentum balance for flow of an incompressible fluid on a rigid wall.

System (2.1) involves five dimensionless parameters. Besides the Reynolds, Froude, Weber and Darcy numbers, Re , Fr , We and Da ,

$$Re = \frac{H_N U_N}{\nu}, \quad Fr = \frac{U_N}{\sqrt{g \sin \theta H_N}}, \quad We = \frac{\sigma}{\rho H_N U_N^2}, \quad Da = \frac{\kappa_x H}{H_N^2}, \quad (2.2a-d)$$

we define an anisotropy parameter ξ as

$$\xi = \kappa_{xH} / \kappa_{yH}, \quad (2.3)$$

which compares the permeabilities in the bulk of the porous medium. The characteristic scales for length and velocity, H_N and U_N , respectively, are chosen to correspond to the total thickness of the entire porous and liquid layers, and to the free-surface velocity of the uniform film which characterises the wavy motion of the free surface. The governing equations have been made dimensionless with a pressure scale equal to $\rho g H_N$, as the flow is driven by gravity. It is useful to introduce the Kapitza number $Ka = \sigma / [\rho \nu^{4/3} (g \sin \theta)^{1/3}] = We Fr^{4/3} Re^{2/3}$, which compares surface tension, viscosity and gravity. This parameter depends only on the fluid properties and the inclination of the wall.

2.1. Base flow

The base flow corresponds to a film of constant thickness whose stability characteristics are investigated within the framework of linear stability analysis. Let (U_B, P_B) represent the solution for the base flow, then it satisfies

$$\frac{u_{yy}}{\varepsilon(y)} - \frac{u}{\kappa_x(y)} + \frac{Re}{Fr^2} = 0, \quad (2.4a)$$

$$-Re p_y - \frac{\cot \theta Re}{Fr^2} = 0, \quad (2.4b)$$

with the boundary conditions

$$u = 0 \quad \text{at } y = 0, \quad u_y = 0 \quad \text{at } y = H, \quad \text{and } p = 0 \quad \text{at } y = H. \quad (2.4c)$$

We introduce a linear differential operator $L \equiv \partial_{yy} - (\varepsilon/\kappa_x)\text{Id}$ for our convenience to account for the viscous diffusion and viscous drag at the solid phase in the porous medium, where Id refers to the identity operator. By construction, $U_B(y = H) = 1$, as the free-surface velocity of the uniform film solution is the velocity scale. Therefore (2.4a) can be written as

$$Lu = -\frac{Re}{Fr^2} \varepsilon, \quad u(0) = u'(H) = 0, \quad u(H) = 1, \quad (2.5a-c)$$

which is a boundary-value problem with an adjustable parameter Re/Fr^2 in the porous medium depending upon the properties of the medium (porosity and permeability) and the geometry of the flow such that $u(H) = 1$ is satisfied (Samanta *et al.* 2013). The anisotropy of the porous medium does not affect the base flow, which is unidirectional.

We use the AUTO07p software (Doedel *et al.* 2008) to solve (2.5a–c) numerically by continuation. To start the continuation, we have considered the free-surface flow on a rigid wall ($\varepsilon = 1, \kappa_x^{-1} = 0$). We then gradually adjust the porosity and permeability to the desired values. AUTO07p is allowed to adapt the mesh, as it is equipped with a mesh refinement algorithm, so it can easily compute the changes of porosity and permeability at the liquid–porous interface. We have checked for the presence of a sufficient number of mesh points in the transition layer. We have also checked that the thickness of the transitional layer Δ is sufficiently low to ensure that the solution is independent of this parameter.

Figure 2 compares the base-flow solution for different values of the Darcy number and for porous-layer thickness $\delta = 0.5$ (figure 2a) and $\delta = 0.1$ (figure 2b). For all the numerical results presented in this work, the porous region is chosen to be relatively thick, with δ set to 0.5. As stated above, the transitional layer is thin enough with $\Delta = 0.001$ (this value is kept constant for the remainder of this work). Even at a low value of the Darcy number ($Da = 0.001$), a significant flow is observable at the top of the porous layer, even though the velocity profile in the bulk of the porous medium is flat and nearly negligible. Three regions can be considered: two momentum boundary layers (Brinkman sublayers) at the top and bottom of the porous medium, for which a significant shear is observed; and a Darcy region in between, where the velocity is nearly uniform. For higher values of the Darcy number ($Da = 0.01$ and $Da = 0.1$), the shear exerted by the liquid flow affects the flow in the porous medium in its entirety and the Darcy sublayer is removed. The extension of the Brinkman sublayers can be determined by balancing the viscous diffusion $\partial_{yy}u/\varepsilon_H$ and the Darcy drag u/Da , which gives the estimate $\delta_B = \sqrt{Da/\varepsilon_H}$. When the Brinkman sublayers do not invade the whole porous medium, i.e. $\delta_B < \delta/2$, an approximate solution to the base flow is a liquid film on a solid substrate for which the no-slip condition is displaced at $y = 1 - \delta + \delta_B$, which gives the approximate solution

$$\tilde{U}_B = \frac{(\delta - \delta_B - y)(y - 2H + \delta - \delta_B)}{(H - \delta + \delta_B)^2}, \tag{2.6}$$

and therefore

$$\frac{Re}{Fr^2} = -\frac{d^2\tilde{U}_B}{dy^2} \approx \frac{2}{(H - \delta + \delta_B)^2}. \tag{2.7}$$

The base-flow velocity, U_B , the solution to (2.5a–c), is compared to its approximation, \tilde{U}_B , the solution to (2.6), in figure 2(a). An excellent agreement in the liquid region of the flow is observed. Hence, the free-surface instability of a film on a porous substrate can be reduced to the instability of a film on an effective impermeable boundary located at the bottom $y = \delta - \delta_B$ of the top Brinkman layer (Samanta *et al.* 2013). In the next section, we will consider the effect of the anisotropy of the porous substrate on the linear stability of the film.

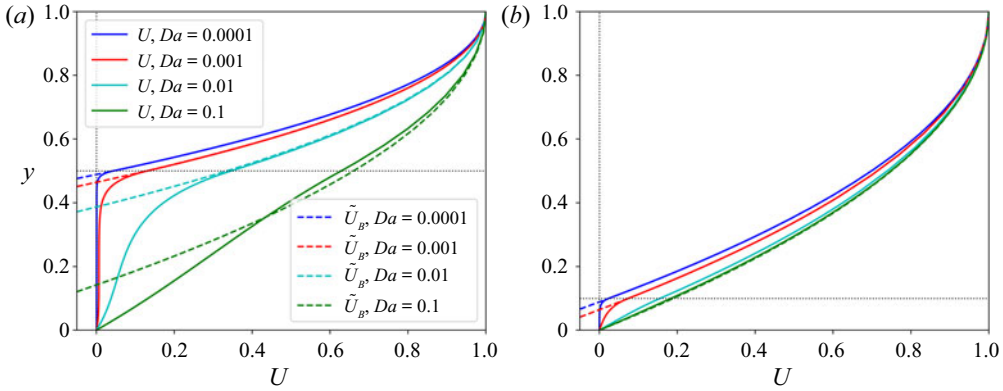


Figure 2. Base-flow velocity profiles $U_B(y)$ and approximated base-flow velocity profiles $\tilde{U}(y)$ as functions of the cross-stream coordinate y for different permeabilities, when $\varepsilon_H = 0.78$, $\Delta = 0.001$, and (a) $\delta = 0.5$ and (b) $\delta = 0.1$.

3. Linear stability analysis

We consider a uniform layer of unit thickness $H = 1$ and introduce a perturbation expansion of the base-flow solution:

$$u(x, y, t) = U_B(y) + ub(x, y, t), \quad v(x, y, t) = vb(x, y, t), \tag{3.1a,b}$$

$$p(x, y, t) = P_B(x) + pb(x, y, t). \tag{3.1c}$$

We further introduce a streamfunction for the perturbation quantities and a modal decomposition with wavenumber $k = k_r + ik_i$ and phase speed $c = c_r + ic_i$,

$$\Psi(x, y, t) = \psi(y) \exp[ik(x - ct)], \tag{3.2}$$

so that $ub = \partial\Psi/\partial y$ and $vb = -\partial\Psi/\partial x$ automatically satisfy the continuity equation for the perturbed flow. The Orr–Sommerfeld boundary-value problem then reads

$$\begin{aligned} (D^2 - k^2)^2 \psi = ik \operatorname{Re} \left[\left(\frac{U_B}{\varepsilon} - c \right) (D^2 - k^2) \psi - \frac{U_B'' \psi}{\varepsilon} + 3U_B' \frac{\varepsilon' \psi}{\varepsilon^2} + U_B \frac{\psi \varepsilon''}{\varepsilon^2} \right. \\ \left. - 3U_B \frac{\psi \varepsilon'^2}{\varepsilon^3} - \left(\frac{U_B}{\varepsilon} - c \right) \frac{\varepsilon' \psi'}{\varepsilon} \right] + \frac{\varepsilon'}{\varepsilon} (D^3 - k^2 D) \psi + \frac{\varepsilon \psi''}{\kappa_x(y)} - \frac{\varepsilon k^2 \xi \psi}{\kappa_x(y)} \\ + \varepsilon \psi' \frac{\partial}{\partial y} \left(\frac{1}{\kappa_x(y)} \right) + \frac{\varepsilon'}{\varepsilon} \psi''' + \frac{\varepsilon''}{\varepsilon} \psi'' - 2 \frac{\varepsilon'^2}{\varepsilon^2} \psi'' - k^2 \frac{\varepsilon'}{\varepsilon} \psi', \end{aligned} \tag{3.3a}$$

along with the boundary conditions

$$\psi|_0 = 0, \quad \psi'|_0 = 0, \tag{3.3b}$$

$$\psi''|_1 + k^2 \psi|_1 = U_B''|_1 \frac{\psi|_1}{(U_B|_1 - c)}, \tag{3.3c}$$

$$\begin{aligned} \psi'''|_1 - 3k^2 \psi'|_1 = i \operatorname{Re} k [(U_B|_1 - c) \psi'|_1 - U_B'|_1 \psi|_1] \\ + ik \left(\cot \theta \frac{\operatorname{Re}}{Fr^2} + k^2 We \operatorname{Re} \right) \frac{\psi|_1}{(c - U_B|_1)}, \end{aligned} \tag{3.3d}$$

where $\varepsilon(1) = 1$ and $1/\kappa(1) = 0$ have been used to simplify the continuity of the normal stress (3.3d). The symbol D and primes refer to derivatives with respect to the cross-stream

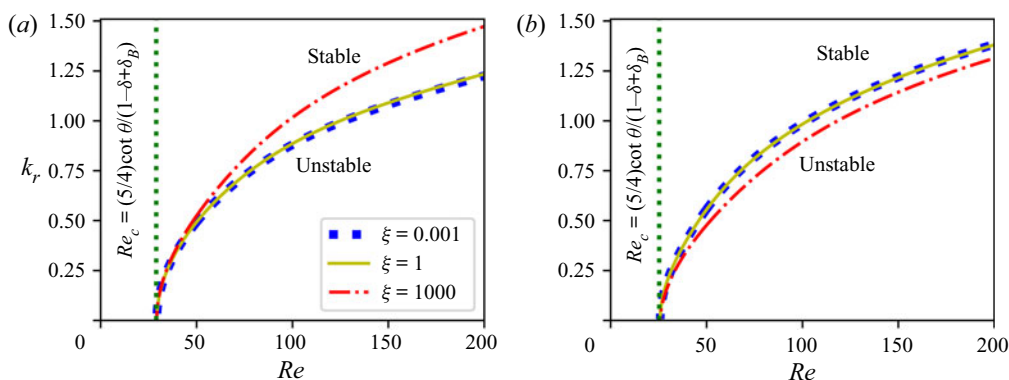


Figure 3. Marginal stability curves corresponding to the Orr–Sommerfeld eigenvalue problem for different permeabilities and different anisotropy parameters, when $\varepsilon_H = 0.78$, $\delta = 0.5$, $\Delta = 0.001$, $\theta = 4.6^\circ$ and $Ka = 769.8$: (a) $Da = 0.001$ and (b) $Da = 0.01$.

coordinate y . The last four terms in (3.3a) can be referred to as the Brinkman second-order correction terms. These terms arise only in the thin transitional region and are negligibly small, so, in our calculation, we ignored these terms (Brinkman 1949). The above boundary-value problem is actually an eigenvalue problem for the complex phase speed c . This eigenvalue problem is solved with AUTO07p for different inclination angles and different anisotropies ξ of the porous plate. We only looked for the surface instability modes, starting our continuation procedure at the trivial solution for $k = 0$.

We first consider the spatial stability of a film on a slightly inclined porous plane for a set of parameters corresponding to an experiment by Liu, Schneider & Gollub (1995), $\theta = 4.6^\circ$, $\sigma = 69 \text{ N m}^{-1}$, $\rho = 1130 \text{ kg m}^{-3}$ and $\nu = 5.02 \times 10^{-6} \text{ m}^2 \text{ s}^{-1}$, which gives $Ka = 769.8$. We thus consider a real angular frequency $\omega = kc$, the instability of the film being signalled by a positive spatial growth rate, i.e. $-k_i > 0$. Figure 3 presents a typical marginal stability curve ($-k_i = 0$) in the Reynolds number Re versus wavenumber k_r plane. As expected, the threshold of the free-surface instability occurs at $k = 0$ for a critical value of the Reynolds number, which depends on the inclination of the plane and the properties of the porous medium. Note that anisotropy does not affect the base flow and appears in (3.3a) only through the product $k^2\xi$. As a consequence, the threshold of the long-wave instability of the film is not affected by the anisotropy of the porous medium and remains equal to its value for the isotropic case $\xi = 1$, where the instability threshold closely corresponds to the case of an effective no-slip condition achieved at the bottom of the top Brinkman momentum diffusion layer, i.e. at $y = 1 - \delta + \delta_B$. In this case, the threshold of instability corresponds to a liquid film of thickness $1 - \delta + \delta_B$, which gives, for our set of parameters,

$$Re_c \approx \frac{5}{4} \frac{\cot \theta}{1 - \delta + \delta_B}. \tag{3.4}$$

The prediction (3.4) of the instability threshold is indicated by vertical lines on figure 3, in striking agreement with our numerical findings.

Figure 4 presents the spatial growth rate $-k_i$ for $Re = 50$ as a function of k_r (recall that $\omega_i = 0$) and shows the influence of the anisotropy parameter. In the isotropic case $\xi = 1$, raising the mean permeability ($Da = 0.01$) enhances the range of the unstable wavenumber window and the spatial growth rate. Higher mean permeability corresponds

Falling film on an anisotropic porous medium

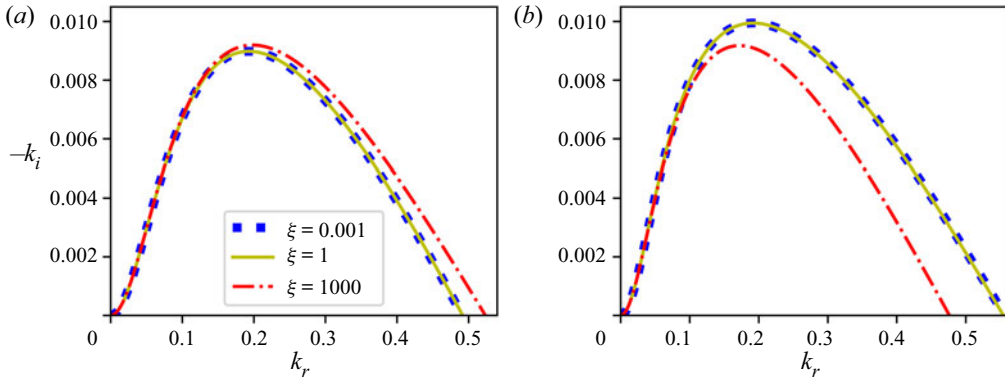


Figure 4. Spatial growth rate for different permeabilities and different anisotropy parameters, when $\varepsilon_H = 0.78$, $\delta = 0.5$, $\Delta = 0.001$, $\theta = 4.6^\circ$, $Ka = 769.8$ and $Re = 50$: (a) $Da = 0.001$ and (b) $Da = 0.01$.

to larger Brinkman layers and thicker effective thickness $1 - \delta + \delta_B$. As a consequence, in the vicinity of the porous–fluid interface, the liquid accelerates and the convective transport in the liquid layer is enhanced, which has a clear destabilising effect.

A low cross-stream permeability ($\xi \gg 1$) affects the stability of the film differently at low ($Da = 0.001$) and moderate ($Da = 0.01$) permeabilities, as can be observed from figures 3 and 4. The isotropic case ($\xi = 1$) is compared to high cross-stream permeability ($\xi = 0.001$) and low cross-stream permeability ($\xi = 1000$) cases. Anisotropy affects the growth rate and phase velocity only for the larger values of the wavenumber k_r , again owing to the fact that ξ is grouped with k^2 in a single term of (3.3a). This dual effect is a consequence of the organisation of the flow in the porous layer into three distinct sublayers: the top and bottom Brinkman layers, for which the shear of the base-flow velocity is significant; and the Darcy sublayer, where a plug flow is observed (cf. figure 2). Raising the anisotropy parameter ξ promotes the drag of the solid matrix (proportional to ξ/Da), which prevents the exchange of mass between the liquid and porous regions. As a consequence, the flow in the Darcy sublayer is almost a constant plug flow, irrespective of the film-height fluctuations. Conversely, in the top Brinkman sublayer, raising ξ promotes the viscous diffusion of film-height fluctuations as a consequence of the continuity of the streamwise velocity at the liquid–porous interface. The result is a reduction of viscous damping of the waves in the Darcy sublayer, whereas the opposite is true in the Brinkman top sublayer. The net balance of these two adverse effects depends on the respective extensions of the Darcy and Brinkman sublayers. At $Da = 0.001$, the Brinkman sublayers are thin ($\delta_B \approx 0.04$) and the destabilising contribution of mitigating streamwise viscous diffusion in the Darcy sublayer dominates. Conversely, at $Da = 0.01$, the Darcy sublayer is absent, as can be observed from figure 2 and the damping effect of an enhanced diffusion in the Brinkman top sublayer dominates.

However, a film flowing on a porous substrate with high cross-stream permeability, i.e. $\xi \ll 1$, presents stability that is equivalent to a flow on an isotropic porous medium, as the marginal stability curves, growth rates and phase speeds are identical at $\xi = 1$ and $\xi = 0.001$. Indeed, lowering the anisotropy parameter ξ below one has no effect on the stability of the film, the viscous damping of the film-height fluctuations in the porous medium then being governed by the streamwise permeability instead of the cross-stream one.

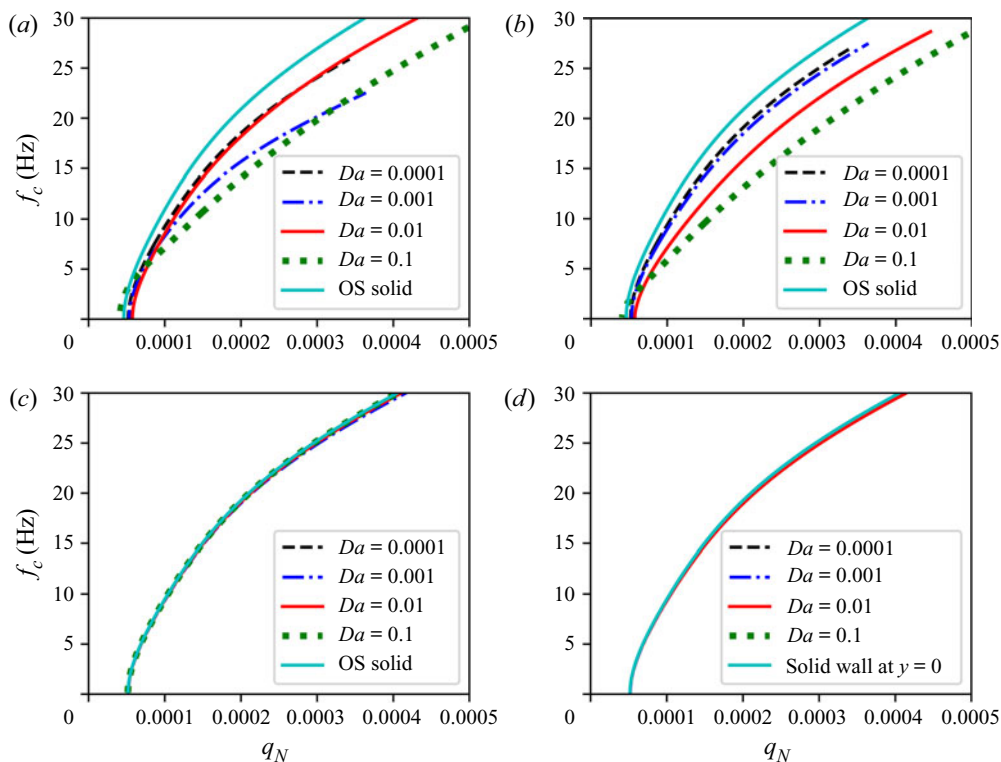


Figure 5. Marginal stability curves for different thicknesses of an anisotropic porous layer for different Darcy values and different ξ values: dimensional cut-off frequency f_c versus dimensional flow rate q_N , for $\varepsilon_H = 0.78$, $\Delta = 0.001$, $\theta = 4.6^\circ$ and (a) $\delta = 0.5$, $\xi = 1$, (b) $\delta = 0.5$, $\xi = 1000$, (c) $\delta = 0.1$, $\xi = 1$ and (d) $\delta = 0.1$, $\xi = 1000$. ‘OS solid’ refers to an impermeable no-slip boundary.

Samanta *et al.* (2013) stated that the stability of a film on a porous media is equivalent to the stability of a liquid film on an impermeable effective boundary located at $y = \delta - \delta_B$, where the Brinkman layer thickness is defined by $\delta_B = \sqrt{Da/\varepsilon_H}$; hereinafter we refer to this model as the ‘no-slip model’.

Figure 5 presents the marginal stability curves when recast in the plane of dimensional flow rate q_N versus dimensional frequency. For a thin porous layer ($\delta = 0.1$), we recover the results obtained by Samanta *et al.* (2013) for the isotropic case ($\xi = 1$). All the curves collapse onto a single curve irrespective of the value of the Darcy number. This curve corresponds to the stability of a liquid film on a solid plate. We conclude that, for thin porous layers, a film flowing on a porous substrate follows the same dynamics as a film on a solid impermeable substrate. However, for a thicker porous region ($\delta = 0.5$), the marginal stability curves present noticeable differences, the permeability of the porous medium significantly promoting the stability of the flow, except close to the instability threshold. Mass exchange at the liquid–porous boundary plays a role in mitigating the instability far from its threshold, as the viscous diffusion in the porous medium can then contribute to the attenuation of velocity fluctuations.

At a large permeability ($Da = 0.1$), the instability occurs at a lower flow rate than for the solid-wall situation. This slight discrepancy in the instability threshold is a consequence of the large difference observed for the velocity profiles (see figure 2). We observe

again that lowering the cross-stream permeability Da/ξ has a dual influence: augmenting the range of unstable frequencies for Da below 0.001, and reducing it above 0.01. At $Da = 0.1$, however, the observed reduction of unstable frequencies is very moderate. A low cross-stream permeability inhibits mass exchange between the porous and liquid layers, decouples the flows in these two layers and prevents the damping of film-height fluctuations by viscous diffusion in the Darcy sublayer. However, due to the continuity of velocity at the porous–liquid interface, the Brinkman top sublayer contributes more efficiently to the damping of the film-height fluctuations. The net balance of these two contributions depends on the relative extensions of the Darcy and Brinkman sublayers. We note that, at $Da = 0.1$ and $\xi = 1000$, the cross-stream permeability is not low enough to efficiently contribute to the damping of short waves, which is then controlled principally by surface tension and the viscous diffusion in the liquid layer.

4. Weighted residual modelling

In this section, a semi-analytic model is derived to capture the long-wave wavy regime of the film flow. The procedure relies on choosing a set of variables whose evolution mimics the complete dynamics of the flow. The total height (porous medium + film) $H = h + \delta$ and the local flow rate $q = \int_0^H u \, dy$ are chosen to characterise the flow evolution. We show in §§ 4.4 and 5 that this strategy is inadequate when a low cross-stream permeability of the porous medium (high values of ξ) is considered. As we underline below, this deficiency results from a decoupling between the flow in the porous and liquid regions.

4.1. Three-equation model

We introduce two different flow rates to allow for the velocity distribution in the porous medium to be decoupled from that in the liquid. We define

$$q_l = \int_0^H Id_l u \, dy \quad \text{and} \quad q_p = \int_0^H Id_p u \, dy, \quad (4.1a)$$

with

$$Id_l = 0.5 + 0.5 \tanh[(y - \delta)/\Delta] \quad \text{and} \quad Id_p = 0.5 - 0.5 \tanh[(y - \delta)/\Delta], \quad (4.1b)$$

so that $Id_l = 1$ and $Id_p = 0$ in the liquid region and conversely $Id_l = 0$ and $Id_p = 1$ in the porous medium. Thus, $q_l \approx \int_\delta^H u \, dy$ is the local discharge of liquid above the porous–liquid interface $y = \delta$, and $q_p \approx \int_0^\delta u \, dy$ is the rate of liquid flowing in the porous medium. Since $Id_l + Id_p = 1$, the total flow rate q is equal to the sum of q_l and q_p . Integrating the continuity equation (2.1a) across the fluid and the porous layer, we get the exact mass balance

$$\partial_t H + \partial_x (q_l + q_p) = 0. \quad (4.2)$$

Two evolution equations can be obtained for q_l and q_p using the weighted residual technique once a velocity profile is assumed (closure assumption). We consider slow space and time evolutions $\partial_{x,t} \sim \gamma$, where γ is a formal small parameter that counts the order of derivation with respect to time and space of the different variables. The velocity distribution across the porous and fluid layers is assumed to remain close to the Nusselt

flat-film distribution, deviations from the Nusselt profile being $O(\gamma)$ corrections induced by the free-surface deformations. We thus decompose u into

$$u = q_l(x, t) f_l(y; H(x, t)) + q_p(x, t) f_p(y; H(x, t)) + \gamma \tilde{u}. \tag{4.3}$$

We use the linearity of the equations (2.5a–c) satisfied by the base flow to write the velocity profile as the superposition of two solutions to

$$L f_i = -C_{ij} \text{Id}_j, \tag{4.4a}$$

where L refers again to the operator $\partial_{yy} - (\varepsilon/\kappa_x)\text{Id}$. For convenience, we have written the above equation in a condensed format using Einstein notation, where $i, j = l$ or p and repetition of indices indicates summation. The associated boundary conditions are

$$f_i(0) = f_p(0) = 0 \quad \text{and} \quad \partial_y f_l(H) = \partial_y f_p(H) = 0. \tag{4.4b}$$

The constants C_{ij} are adjusted to satisfy the integral constraints

$$\int_0^H \text{Id}_i f_j \, dy = \delta_{ij}, \tag{4.4c}$$

implied by the definition (4.1) of the variables q_l and q_p . Here δ_{ij} refers to the Kronecker delta function. Constants C_{ij} are therefore dependent on the geometry of the porous medium and therefore are functions of the film height H . The decomposition (4.3) is made unique with the two gauge conditions

$$\int_0^H \text{Id}_i \tilde{u} \, dy = 0, \tag{4.4d}$$

which guarantee that the decomposition (4.3) satisfies the definitions (4.1) of the flow rates q_l and q_p in the liquid and porous layers.

The momentum balances (2.1b) and (2.1c) are next simplified within the framework of the long-wave expansion to yield a Prandtl-like equation after elimination of the pressure field. From the continuity equation (2.1a) we get $v = -\int_0^y \partial_x u \, dy = O(\gamma)$, so that inertial terms in the cross-stream momentum balance equation (2.1c) are $O(\gamma^2)$ and can be omitted. Integration of (2.1c) thus gives

$$\begin{aligned} Re \, p = & 2\partial_y v|_H - Re \, We \, \partial_{xx} H + \int_H^y \frac{1}{\varepsilon(y)} L v \, dy + (1 - \xi) \int_H^y \frac{v}{\kappa} \, dy \\ & - \frac{Re}{Fr^2} \cot \theta (y - H) + O(\gamma^2), \end{aligned} \tag{4.5}$$

where the leading-order contribution from surface tension, $-We \, Re \, \partial_{xx} H$, has been retained, although it is formally $O(\gamma^2)$, since surface tension prevents the breaking

of waves. Substituting (4.5) into (2.1b), we get the boundary-layer equation

$$\begin{aligned}
 & Re \left[u_t + \frac{1}{\varepsilon}(uu_x + vu_y) + uv \frac{\partial}{\partial y} \left(\frac{1}{\varepsilon} \right) \right] \\
 &= \varepsilon \left[\frac{Re}{Fr^2}(1 - \cot \theta H_x) + Re We H_{xxx} \right] - \varepsilon(y) \frac{\partial}{\partial x} \int_H^y \frac{1}{\varepsilon} Lv \, dy \\
 &\quad - \varepsilon(1 - \xi) \frac{\partial}{\partial x} \int_H^y \frac{v}{\kappa} \, dy + u_{xx} + Lu + 2\varepsilon \frac{\partial}{\partial x}(u_x|_H), \tag{4.6}
 \end{aligned}$$

with the associated boundary conditions

$$u|_0 = v|_0 = 0, \tag{4.7a}$$

$$\partial_y u|_H = 4\partial_x u|_H \partial_x H - \partial_x v|_H, \quad v|_H = \partial_t H + u|_H \partial_x H. \tag{4.7b}$$

Following the weighted residual method, we insert (4.3) into the truncated momentum balance (4.6) and average it with weights that satisfy

$$Lw_i = -\frac{Re}{Fr^2} Id_i, \quad w_i(0) = \partial_y w_i(H) = 0. \tag{4.8a,b}$$

This choice of weights enables us to make use of the gauge conditions (4.4d) to get rid of the $O(\gamma)$ corrections arising from the evaluation of the viscous terms:

$$\int_0^H w_i Lu \, dy = w_i(H) \partial_y u|_H + \int_0^H Lw_i u \, dy = w_i(H) [4u_x|_H H_x - v_x|_H] - \frac{Re}{Fr^2} q_i. \tag{4.9}$$

We finally obtain two averaged momentum balances of the form

$$\begin{aligned}
 S_i^{(k)} \partial_t q_i &= -F_{ij}^{(k)} \frac{q_j}{H} \partial_x q_i + G_{ij}^{(k)} \frac{q_j q_i}{H^2} \partial_x H + \frac{1}{Fr^2} \left[I^{(k)} b(H) H - \frac{qk}{H^2} \right] \\
 &\quad + \frac{1}{Re} \left[(J_i^{(k)} + \xi \tilde{J}_i^{(k)}) \frac{q_i}{H^2} (\partial_x H)^2 - (K_i^{(k)} + \xi \tilde{K}_i^{(k)}) \frac{\partial_x q_i \partial_x H}{H} \right. \\
 &\quad \left. - (L_i^{(k)} + \xi \tilde{L}_i^{(k)}) \frac{q_i}{H} \partial_{xx} H + (M_i^{(k)} + \xi \tilde{M}_i^{(k)}) \partial_{xx} q_i \right], \tag{4.10}
 \end{aligned}$$

where $b(H) = 1 - \cot \theta \partial_x H + We Fr^2 \partial_{xxx} H$ combines the gravitational and the pressure gradient that drive the flow. Equations (4.2) and (4.10) form a three-equation system of evolution equations for the three variables H , q_l and q_p .

All 54 coefficients involved in (4.10) depend on the geometry and therefore on H . The expressions of the coefficients are given in Appendix A. We used the software AUTO07p to compute (4.4), (4.8a,b) and (A1) and tabulated the coefficients (A2) as a function of the film height H .

The derived system of equations is consistent up to order γ for convective terms and up to $O(\gamma^2)$ for diffusion terms. We underline that consistency up to $O(\gamma)$ is a requisite to ensure that the instability threshold is captured adequately. Inclusion of viscous diffusion terms enables one to recover correctly the amplitude of the capillary ripples, which precede hump waves and solitary waves and govern their dynamics.

4.2. Two-equation models

The three-equation model (4.2) and (4.10) will be contrasted with the two-equation approach adopted in Samanta *et al.* (2013). Choosing the film elevation H and the total flow rate $q = q_l + q_p$ as the set of variables, a set of evolution equations can be obtained with the above weighted residual method with the ansatz

$$u = qf(y; H) + \gamma\tilde{u}, \tag{4.11}$$

where f corresponds to the base-flow profile U_B and satisfies

$$Lf = -C, \quad f(0) = 0, \quad \partial_y f(H) = 0, \quad \int_0^H f \, dy = 1. \tag{4.12a-d}$$

The same procedure as that outlined in §4.1 is then followed with a weight defined by

$$Lw = -\frac{Re}{Fr^2}, \quad \partial_y w(H) = 0. \tag{4.13a,b}$$

Integrating (4.6) with the weight w then leads to

$$\begin{aligned} S(H)\partial_t q &= -F(H)\frac{q}{H}\partial_x q + G(H)\frac{q^2}{H^2}\partial_x H + \frac{1}{Fr^2} \left[I(H)b(H)H - \frac{q}{H^2} \right] \\ &+ \frac{1}{Re} \left[(J(H) + \xi\tilde{J}(H))\frac{q}{H^2}(\partial_x H)^2 - (K(H) + \xi\tilde{K}(H))\frac{\partial_x q \partial_x H}{H} \right. \\ &\left. - (L(H) + \xi\tilde{L}(H))\frac{q}{H}\partial_{xx} H + (M(H) + \xi\tilde{M}(H))\partial_{xx} q \right]. \end{aligned} \tag{4.14}$$

The expressions of the coefficients from $S(H)$ to $\tilde{M}(H)$ correspond to (A1) and (A2) once indices have been dropped out. For an isotropic porous medium $\xi = 1$, the averaged momentum balance (4.14) is fully identical to the corresponding one obtained by Samanta *et al.* (2013), as the differences in the expressions of the coefficients arise from a different choice of writing the ansatz (4.11) which does not affect the result.

4.3. Approximation

In order to get a more easily handled model, we propose here a drastic simplification of our modelling attempt. This simplification relies on a polynomial approximation of the velocity profiles f_i and weights w_i (i referring to either l or p). To proceed, we separate the flow into three regions: a Brinkman sublayer of thickness $\delta_B = \sqrt{Da/\varepsilon_H}$ at the bottom of the porous layer; a uniform-flow Darcy region in the bulk of the porous layer from $y = \delta_B$ to $y = \delta - \delta_B$; and an effective liquid layer from $y = \delta - \delta_B$ to the top of the film flow $y = H$. We thus approximate f_i and w_i as

$$\left. \begin{aligned} f_i &= a_i y, & w_i &= a_{wi} y, & \text{for } 0 \leq y \leq \delta_B, \\ f_i &= a_i \delta_B, & w_i &= a_{wi} \delta_B, & \text{for } \delta_B \leq y \leq \delta - \delta_B, \\ f_i &= a_i \delta_B + b_i \tilde{U}_B, & w_i &= a_{wi} \delta_B + b_{wi} \tilde{U}_B, & \text{for } y \geq \delta - \delta_B, \end{aligned} \right\} \tag{4.15}$$

where \tilde{U}_B is given by (2.6). This approximation implies that the operator L reduces to ∂_{yy} in the Brinkman sublayers $\delta - \delta_B \leq y \leq \delta$ and to $-(\varepsilon_H/Da)\text{Id}$ in the Darcy layer, or

bulk, of the porous layer. This approximation also assumes that the transitional layer has a negligible thickness and that the thickness of the Brinkman sublayer δ_B is small.

Approximation (4.15) yields explicit expressions for the coefficients (A2), of which we retain only the leading-order contributions or up to $O(\delta_B)$. Additionally, the flow rate in the porous layer q_p can be inferred to be proportional to the Darcy number, so that $q_p = O(\delta_B^2)$ is small and the corresponding coefficients are truncated to their leading order with respect to δ_B . Since the velocity distribution in the liquid layer and the top Brinkman sublayer $\delta \leq y \leq \delta - \delta_B$ is close to the velocity distribution of a liquid film on a solid interface at $y = \delta - \delta_B$, we introduce the effective film thickness $h = H - \delta + \delta_B$ and the effective thickness of the porous medium $\tilde{\delta} = \delta - \delta_B$. We obtain explicit expressions for the coefficients, which are listed in Appendix B.

The averaged momentum balances can be further simplified by considering $q_p = O(Da)$ and keeping leading-order terms for $Da \ll 1$. We thus retain terms involving the anisotropy parameter ξ up to $O(\xi Da^{3/2})$:

$$\begin{aligned} \partial_t q_l - \frac{h}{6\tilde{\delta}} \partial_t q_p = & -\frac{17}{7} \frac{q_l}{h} \partial_x q_l + \frac{9}{7} \frac{q_l^2}{h^2} \partial_x h + \frac{1}{Fr^2} \left[\frac{5h}{6} b(h) - \frac{5(1 - \tilde{\delta})^2}{4h^2} q_l \right] \\ & + \frac{1}{Re} \left\{ \left[4 - \frac{3}{2} \xi \left(\frac{\delta_B}{h} \right)^3 \right] \frac{q_l (\partial_x h)^2}{h^2} - \left[\frac{9}{2} - \xi \left(\frac{\delta_B}{h} \right)^3 \right] \frac{\partial_x q_l \partial_x h}{h} \right. \\ & - \left[6 - \frac{1}{2} \xi \left(\frac{\delta_B}{h} \right)^3 \right] \frac{q_l}{h} \partial_{xx} h + \left[\frac{9}{2} - \frac{1}{4} \xi \left(\frac{\delta_B}{h} \right)^3 \right] \partial_{xx} q_l \\ & \left. + \frac{5}{12} \xi \frac{\delta_B}{h} \partial_{xx} q_p \right\}, \end{aligned} \tag{4.16a}$$

and

$$\begin{aligned} \partial_t q_l + \partial_t q_p = & -\frac{12}{5} \frac{q_l}{h} \partial_x q_l + \frac{6}{5} \frac{q_l^2}{h^2} \partial_x h + \frac{1}{Fr^2} \left[(h + \tilde{\delta} \varepsilon_H) b(h) - \frac{(1 - \tilde{\delta})^2 \varepsilon_H}{2Da} q_p \right] \\ & + \frac{1}{Re} \left\{ \left[\frac{3(2h + \tilde{\delta} \varepsilon_H)}{h} - 3\xi \frac{\tilde{\delta}^2}{h^2} \right] \frac{q_l (\partial_x h)^2}{h^2} \right. \\ & + \left[-\frac{3(2h + \tilde{\delta} \varepsilon_H)}{h} + 2\xi \frac{\tilde{\delta}^2}{h^2} \right] \frac{\partial_x q_l \partial_x h}{h} + \left[-\frac{3(4h + \tilde{\delta} \varepsilon_H)}{2h} + \xi \frac{\tilde{\delta}^2}{h^2} \right] \frac{q_l}{h} \partial_{xx} h \\ & \left. + \frac{1}{2} \left[9 + \frac{3\tilde{\delta} \varepsilon_H}{h} - \frac{\xi \tilde{\delta}^2}{h^2} \right] \partial_{xx} q_l + \frac{\xi \tilde{\delta}^2 \varepsilon_H}{3 Da} \partial_{xx} q_p \right\}. \end{aligned} \tag{4.16b}$$

These are completed by the mass balance rewritten in terms of h , q and q_p , i.e.

$$\partial_t h + \partial_x (q_l + q_p) = 0. \tag{4.17}$$

The influence of anisotropy on the momentum balance in the liquid layer (4.16a) is weak, as all terms involving ξ in this equation are functions of the ratio of the extensions of the Brinkman sublayer and liquid layer δ_B/h . These terms originate from the solid-matrix drag

occurring in the Brinkman top sublayer. More precisely, these terms arise from the integral

$$\int_0^H w_l \varepsilon \xi \partial_x \left(\int_H^y \frac{v}{\kappa} dy \right) dy \approx \int_{\delta-\delta_B}^\delta w_l \varepsilon \xi \partial_x \left(\int_H^y \frac{v}{\kappa} dy \right) dy, \tag{4.18}$$

since $1/\kappa = 0$ in the liquid region and the weight function w_l , defined by (4.13a,b), is nearly zero in the Darcy sublayer, and set to zero in the approximation (4.15). Considering that all terms involving ξ in (4.16a) are at most $O(\xi \delta_B^3)$, since $q_p = O(\delta_B^2)$, provides a criterion at which viscous diffusion in the Brinkman sublayer becomes significant, i.e. $\xi Da^{3/2} = O(1)$.

From (4.16b), we can expect an efficient diffusion of the flow rate in the porous medium in the case of a weak cross-stream dimensionless permeability Da/ξ . One limit is then worthy of interest, i.e. $q_p \rightarrow \text{const.}$, which may be achieved when $\xi/Da \gg 1$.

Considering simultaneously $\xi Da^{3/2} \ll 1$ and $\xi/Da \gg 1$ yields

$$\begin{aligned} \partial_t q_l = & -\frac{17}{7} \frac{q_l}{h} \partial_x q_l + \frac{9}{7} \frac{q_l^2}{h^2} \partial_x h + \frac{1}{Fr^2} \left[\frac{5h}{6} b(h) - \frac{5(1-\tilde{\delta})^2}{4h^2} q_l \right] \\ & + \frac{1}{Re} \left\{ 4 \frac{q_l (\partial_x h)^2}{h^2} - \frac{9}{2} \frac{\partial_x q_l \partial_x h}{h} - 6 \frac{q_l}{h} \partial_{xx} h + \frac{9}{2} \partial_{xx} q_l \right\}, \end{aligned} \tag{4.19}$$

which corresponds to a liquid film flow on an impermeable solid wall at $y = \tilde{\delta} = \delta - \delta_B$ with a no-slip boundary condition. In this case, the wavy motion of the liquid is unaffected by the porous medium. This is a consequence of neglecting the solid-matrix drag occurring in the Brinkman top sublayer and also neglecting the mass exchange at the liquid–porous interface.

The approximate momentum balance (4.19) can also be derived from (4.16a) for isotropic or moderately anisotropic porous media ($\xi = O(1)$) in the limit $q_p \ll 1$, which is achieved at very low permeabilities ($Da \rightarrow 0$) or for thin porous layers (small values of δ).

In the remainder of this paper, we discuss and compare the solutions to the three-equation models (4.2), (4.10), and (4.17), (4.16), and to the two-equation models (4.2), (4.14), and (4.17), (4.19). For convenience, these models are referred to as three-equation full and approximate models, and two-equation full and no-slip models, respectively.

4.4. Linear stability analysis

We next turn to the stability analysis of the flat-film solution based on the three-equation full and approximate models (4.2), (4.10) and (4.17), (4.16), and the two-equation model (4.2), (4.14). We compare our results to the solutions of the Orr–Sommerfeld equations (3.3a) in an attempt to validate our modelling approach.

Figure 6 compares the marginal stability curves of the three- and two-equation models to the Orr–Sommerfeld analysis in the limit of high and low cross-stream permeability (i.e. $\xi = 1$ and $\xi = 1000$, respectively). If the three-equation model satisfactorily reproduces the Orr–Sommerfeld analysis, the two-equation full model does not. This inadequacy is a consequence of the ansatz (4.11), which yields an overestimation of the contribution of the cross-stream permeability on the viscous diffusion of the waves (coefficients $\tilde{L}(1)$ and $\tilde{M}(1)$). We conclude that the three-equation models offer reliable alternatives to the Orr–Sommerfeld analysis and are quite accurate. In the isotropic case ($\xi = 1$) and for

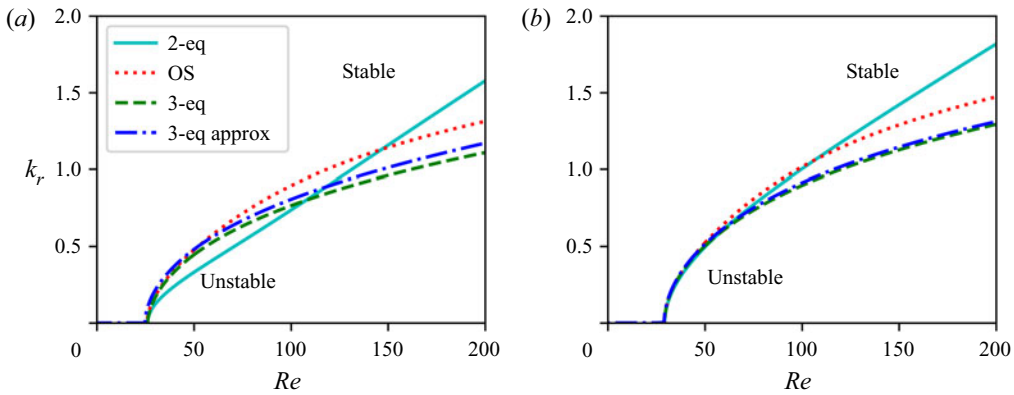


Figure 6. Comparisons of the marginal stability curves for the two-equation full (4.2), (4.14), three-equation full (4.2), (4.10), and approximate model (4.17), (4.16), with the Orr–Sommerfeld analysis. All the curves are plotted with the parameter set $\varepsilon_H = 0.78$, $\delta = 0.5$, $\Delta = 0.001$, $Ka = 769.8$ and $\theta = 4.6^\circ$: (a) $Da = 0.01$, $\xi = 1000$; and (b) $Da = 0.001$, $\xi = 1000$.

relatively large permeability ($Da = 0.01$), the three-equation approximate model is slightly less accurate than the full model, predicting reduced intervals of unstable wavenumbers than the full model and Orr–Sommerfeld analysis. However, this is expected, as the polynomial approximation leading to the approximate model assumes that the base-flow velocity profile presents a constant velocity distribution in the bulk of the porous layer (Darcy sublayer). Such a Darcy sublayer is already not observed at $Da = 0.01$ (cf. figure 2).

5. Nonlinear travelling-wave solutions

We next turn to the construction of the nonlinear TW solutions to the models. These solutions correspond to waves propagating at a constant speed and with a constant shape. The variables are then functions of the coordinate $\zeta = x - ct$ in the moving frame at speed c of the wave. The system of equations then reduces to a set of ordinary differential equations, which are recast into an autonomous dynamical system. The first step is the integration of the mass balance (4.2) with respect to ζ , which gives $q = q_l + q_p = cH + q_0$, where $q_0 = \int_0^H (u - c) dy$ is the constant flow rate in the moving frame of the wave. Substitution of $cH + q_0$ for q then leads to

$$\frac{dU}{d\zeta} = F(U, c), \tag{5.1}$$

where U is a three-dimensional vector $(H, H', H'')^t$ for the two-equation models (4.2), (4.14), and (4.17), (4.19), and a four-dimensional vector $(H, H', H'', q_p)^t$ for the three-equation models (4.2), (4.10), and (4.17), (4.16), the primes denoting derivatives with respect to ζ . The locations of the fixed-point solutions to (5.1) satisfy

$$H^3 \{I^{(l)}(H) + I^{(p)}(H)\} - cH - q_0 = 0, \tag{5.2}$$

where $I^{(l)}$ and $I^{(p)}$ are defined in (A2m), (B1a) and (B1b). Equation (5.2) admits three solutions, of which only two may be positive. Consequently, a maximum of two fixed points is observed in the phase space for any value of the phase speed c .

The moving-frame flow rate q_0 is determined by imposing an integral constraint $\langle q \rangle = I^{(l)}(1) + I^{(p)}(1)$, which corresponds to the conservation of mass in a time-dependent

simulation with open-domain boundary conditions at the outlet and a periodic forcing at the inlet (Scheid *et al.* 2005).

The autonomous dynamical system (5.1) constitutes an integral boundary-value problem. Branches of solutions are constructed by varying c , which is the principal continuation parameter of the computations. In the context of falling-film flows on an impermeable substrate, several studies (Chang, Demekhin & Kopelevitch 1993; Sisoev & Shkadov 1999; Shkadov & Sisoev 2004) have been devoted to obtaining a detailed picture of the different TW branches of solutions to the famous Shkadov model (Shkadov 1967). The first family of γ_1 waves bifurcates from the marginal stability curve through a Hopf bifurcation. These ‘slow’ waves have a speed smaller than that of spatially amplified infinitesimal waves at the same frequency. The corresponding solution branch terminates at small frequency as negative pulses with a deep trough followed by capillary waves. However, the waves experimentally observed at low frequency are ‘fast’ waves, i.e. having speed larger than that of infinitesimal waves, and have a large hump preceded by capillary ripples. This second family of waves (γ_2) bifurcates from a period-doubling bifurcation of the γ_1 branch. By considering the symmetry breaking of a wave made of n identical γ_1 waves, many more branches of solutions, denoted here as γ_n , have been found. Sisoev & Shkadov (1999) showed that the γ_n waves, $n \geq 3$, bifurcate at a low value of Re in pairs of slow and fast waves that terminate at low wavenumber as solitary waves having different numbers of troughs and bumps. On increasing Re , Chang *et al.* (1993) observed a series of pinching of the γ_2 branch of solutions with the γ_n waves.

Different branches of TWs obtained in the conditions of Liu and Gollub’s experiments (Liu, Schneider & Gollub 1995) are displayed in figure 7 at increasing values of the Reynolds number for a fixed inclination $\beta = 4^\circ$ and Kapitza number $\Gamma = 2340$. Among a wide variety of solution branches, we choose to show only those that relate to the branch of fast γ_2 waves. In particular, only the one-humped γ_2 fast waves are displayed, whereas n -humped fast waves can be found. However, one-humped γ_2 waves are always the fastest at a given frequency, and therefore dominate the wave dynamics.

Close to criticality ($Re_c \approx 29.1$) and for the isotropic case ($\xi = 1$), the γ_2 family emerges from a Hopf bifurcation whereas the γ_1 waves appear through a period-doubling bifurcation of the γ_2 waves. This situation is reversed at higher values of Re (compare figure 7*a* and 7*b*). The γ_1 and γ_2 families form an imperfect bifurcation with a permutation of branch connections for $33.8 < Re < 36$. As the Reynolds number is increased, the fast-wave γ_2 branch experiences several collisions with other branches. Figure 7(*c,d*) displays one such pinching, for $42.7 < Re < 45.5$. Each of these pinching events is reminiscent of the imperfect bifurcation affecting the γ_1 and γ_2 wave branches. They give rise to the secondary slow-wave solution branches, denoted by γ_1' and γ_1'' branches in figure 7. The profiles of the waves corresponding to the different branches are illustrated in figure 8 for the frequency $f = 1$ Hz. Figures 8(*b,d*) correspond to slow waves made of one or several troughs followed by capillary oscillations before returning to the level of the flat film. The shape of the high-speed end of the γ_2 branch (figure 8*a*) is different, with a main hump preceded by capillary ripples. The γ_1 waves correspond to a unique trough whereas γ_1' and γ_1'' present several troughs.

Anisotropy significantly affects the sequence of bifurcations and the emergence of TWs. Notably, close to criticality, the slow γ_1 wave branch was not found. At higher values of Re , the sequence of pinching events giving rise to multiple trough-like $\gamma_1^{(n)}$ waves is modified. Raising ξ lowers the wave speed as a result of a more efficient viscous diffusion in the porous medium. It also affects the shape of the waves, as can be observed from figure 8. Large values of ξ correspond to a more efficient viscous diffusion in the

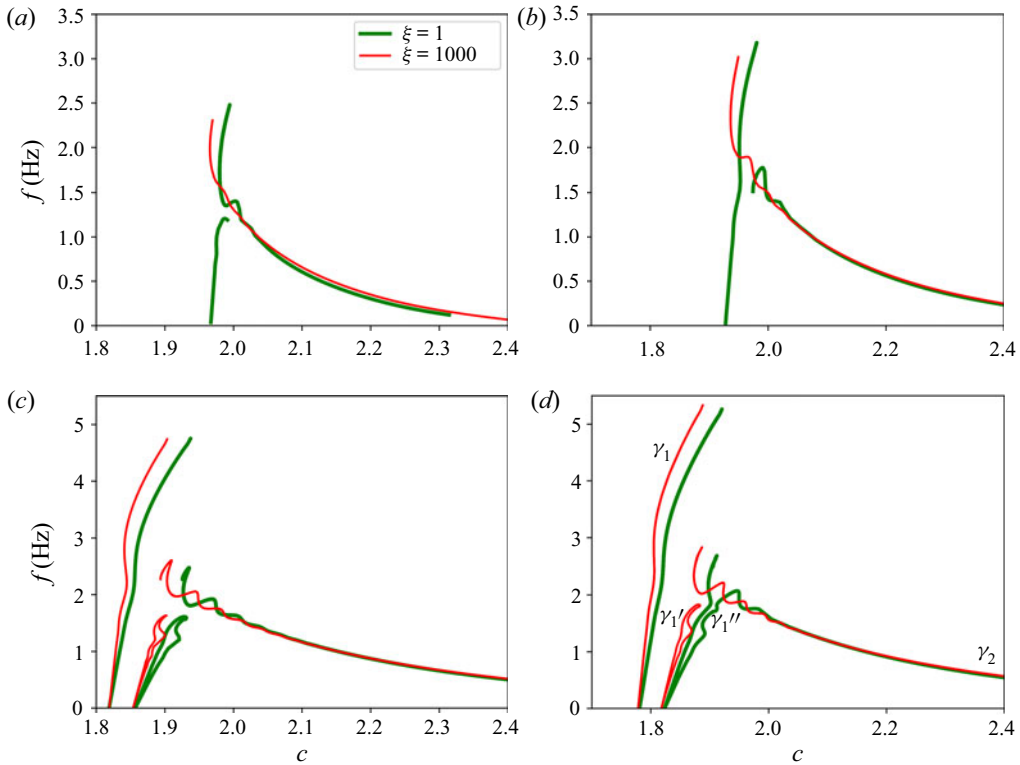


Figure 7. Bifurcation diagrams of the TW solutions to the three-equation full model (4.2), (4.10) in the plane of velocity c versus dimensional frequency f . The Reynolds number $R = q_N/\nu$ based on the flow rate at the inlet is: (a) $Re = 33.8$ ($R = 15$), (b) $Re = 36$ ($R = 16$), (c) $Re = 42.8$ ($R = 19$) and (d) $Re = 45.5$ ($R = 20.2$). Parameters are $Da = 0.01$, $\varepsilon_H = 0.78$, $\delta = 0.5$, $\Delta = 0.001$, $\theta = 4^\circ$, $Ka = 2340$ and $\nu = 2.3 \times 10^{-6} \text{ m}^2 \text{ s}^{-1}$.

Brinkman sublayer, which impacts the amplitude of short capillary waves. The effect of anisotropy on TWs strongly depends on the value of the Darcy number. At $Da = 0.001$, the effect is weak, as can be observed from figure 9. This is expected, as low permeabilities imply weak flows in the porous medium.

The approximate model (4.17), (4.16) captures remarkably well the complex bifurcation diagram of TW solutions and predicts correctly the lowering of the wave speed as the anisotropy parameter is raised from $\xi = 1$ to $\xi = 1000$. In particular, the agreement with the full three-equation model (4.2), (4.10) is convincing even at $Da = 0.01$, which is unexpected, as the derivation of the approximate model requires $Da \ll 1$ (compare figure 10 to figures 7 and 9). However, the obtained bifurcation diagrams show some small discrepancies with the result from the full three-equation model. For instance, the multiple-trough γ_1'' branch connects to a two-hump fast wave branch at $Da = 0.01$ and $\xi = 1$. Note that multiple-hump fast waves can be obtained with the full three-equation model (4.2), (4.10), but have not been displayed for simplification.

Finally, we conclude this section by discussing γ_2 limit cycles of large extensions, which we refer to as ‘solitary waves’, as these waves tend to organise and dominate the time evolution of noise-driven falling films (Chang *et al.* 1993). Figure 11 presents limit cycles of large extensions ($\lambda = 200$) which approach homoclinicity. We compared the solutions to the three-equation full model (4.2), (4.10), and approximate model (4.17),

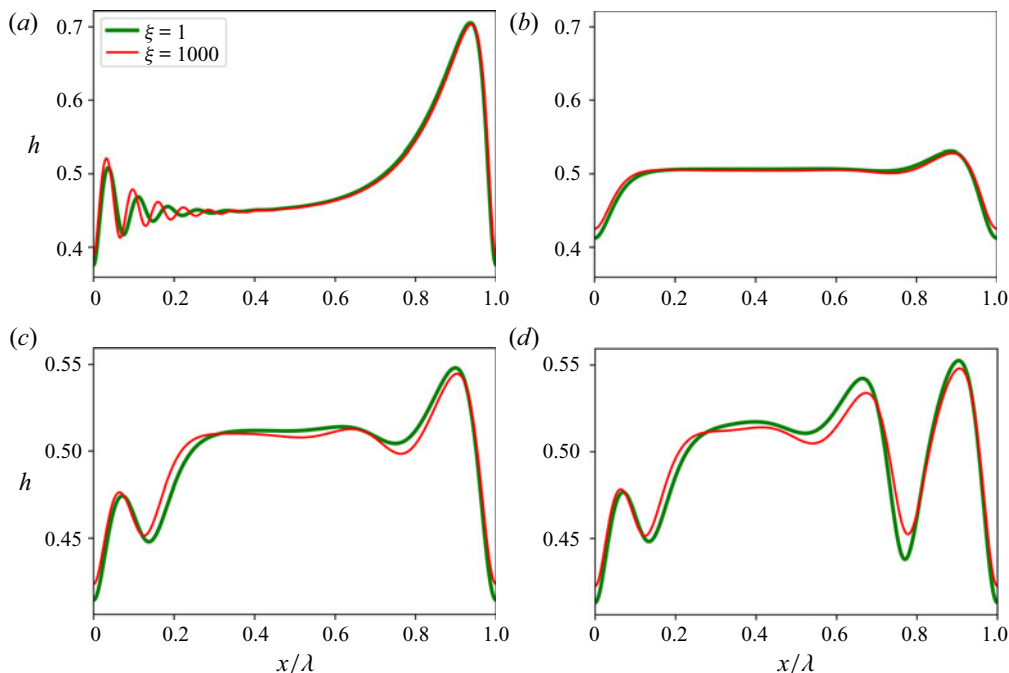


Figure 8. Wave profiles of the TW solutions to the three-equation full model (4.2), (4.10) corresponding to the different wave families indicated in figure 7(d): the (a) γ_2 , (b) γ_1 , (c) γ_1' and (d) γ_1'' wave families. Here λ corresponds to the period. Parameters are $Da = 0.01$, $\varepsilon_H = 0.78$, $\delta = 0.5$, $\Delta = 0.001$, $\theta = 4^\circ$, $Ka = 2340$, $Re = 45.5$ ($R = 20.2$), frequency $f = 1$ Hz and $\nu = 2.3 \times 10^{-6} \text{ m}^2 \text{ s}^{-1}$.

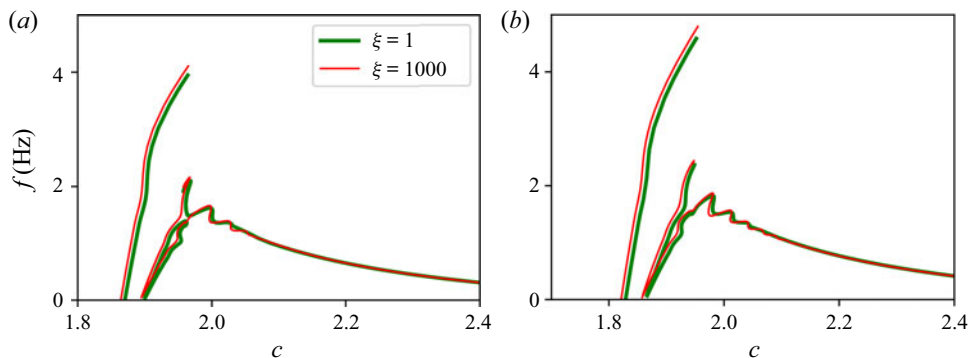


Figure 9. The same as figure 7 except for $Da = 0.001$: (a) $Re = 42.8$ ($R = 19$) and (b) $Re = 45.5$ ($R = 20.2$).

(4.16), and to the two-equation full model (4.2), (4.14), and no-slip model (4.17), (4.19). For a small value of the Darcy number ($Da = 0.001$), a remarkable agreement (not shown) is achieved between the solutions of the full and approximate three-equation models, as the polynomial approximations for the velocity profiles employed in § 4.3 hold in the limit $Da \ll 1$. As the Darcy number is raised to $Da = 0.01$, some departures of the solutions from the approximate model to the full model are noticeable. However, the approximate model remains a convincing substitute for the full model.

Falling film on an anisotropic porous medium

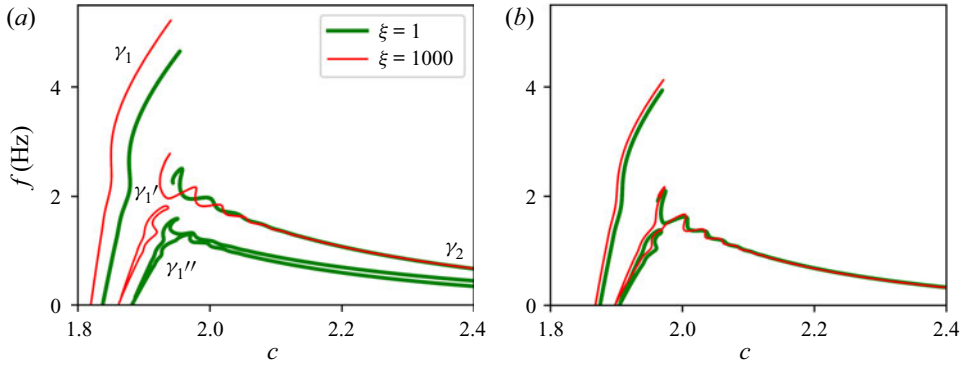


Figure 10. Bifurcation diagrams of the TW solutions to the three-equation approximate model (4.17), (4.16) at $Re = 42.8$: (a) $Da = 0.01$ and (b) $Da = 0.001$. The other parameters are identical to those in figure 7.

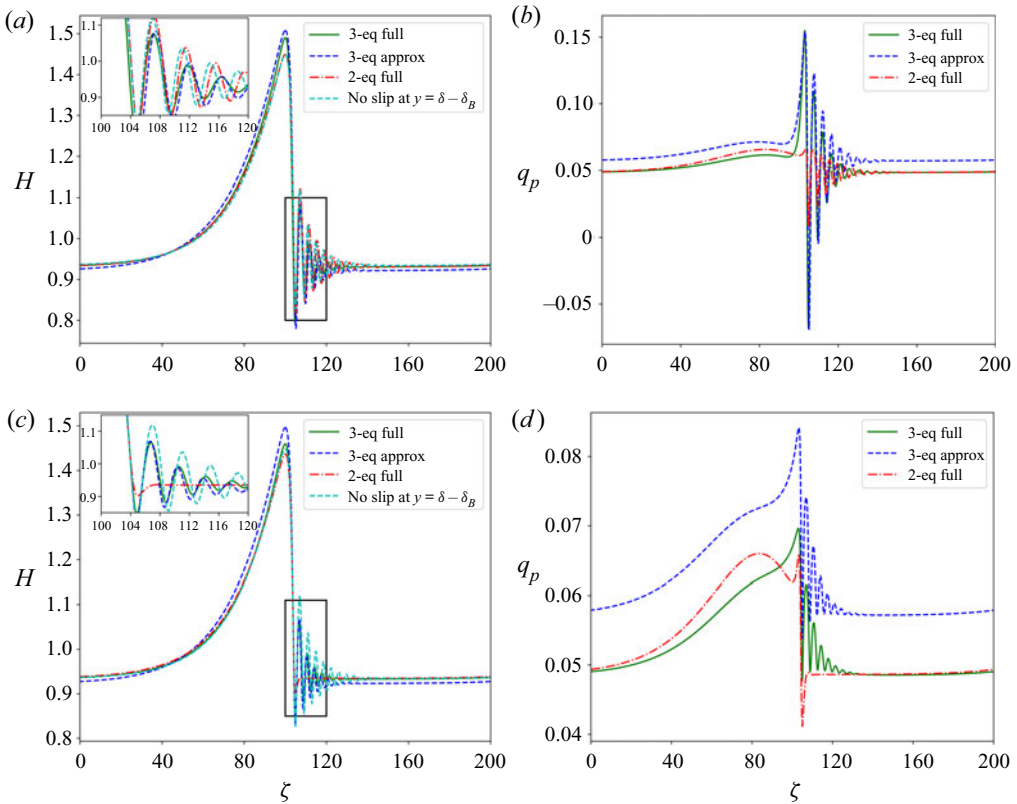


Figure 11. Nonlinear TWs for the two-equation full (4.2), (4.14), and three-equation full (4.2), (4.10), and approximate (4.17), (4.16) models, and for the no-slip model (4.17), (4.19) (impermeable wall at $y = \delta - \delta_B$), when $\varepsilon_H = 0.78$, $\delta = 0.5$, $\Delta = 0.01$, $Ka = 769.8$, $\theta = 4.6^\circ$ and $\lambda = 200$. Here H indicates the thickness of the entire layer (porous and liquid). (a) $Da = 0.01$, $\xi = 1$; (b) $Da = 0.01$, $\xi = 1$; (c) $Da = 0.01$, $\xi = 1000$; and (d) $Da = 0.01$, $\xi = 1000$.

In the case of an isotropic porous medium ($\xi = 1$), the wave profiles obtained with the two-equation full model and the no-slip model nearly collapse onto single curves. This agreement can be comprehended by computing the flow rate in the porous medium $\tilde{q}_p = q \int_0^H Id_p f(y; H) dy$ corresponding to the single velocity profile ansatz (4.11). As can

be observed from [figure 11\(b\)](#), \tilde{q}_p presents moderate fluctuations so that \tilde{q}_p can be assumed somewhat constant. Since $q_p = \text{const.}$ or $q_p \ll 1$ are the conditions yielding the no-slip model, this explains the observed concordance of results from the no-slip and two-equation full model at $\xi = 1$. At $\xi = 1000$, solitary-wave solutions to the two-equation full model present capillary ripples whose number and amplitude are significantly lower than with the other models, to the point that, for $Da = 0.01$, only one capillary ripple is observable at the front of the wave (see [figure 11c](#)). This discrepancy results from the overestimation of the contributions of the porous medium to the viscous diffusion terms in the momentum balance (4.14) implied by the one-velocity ansatz (4.11).

A comparison of the solutions of the three-equation models at $\xi = 1$ and $\xi = 1000$ shows that the fluctuations of the flow rate q_p in the porous medium are efficiently attenuated by lowering the cross-stream permeability (thus raising ξ). This explains the convergence of the solutions to the three-equation and no-slip models at $\xi = 1000$. Finally, let us note that the intensity of the mass exchange between the porous and liquid regions, as reflected by the fluctuations of q_p , is predicted to be much higher with the three-equation models than with the two-equation full model in the isotropic case ($\xi = 1$). We conclude that the assumption of a complete slaving of the velocity distribution in the porous medium to that in the liquid medium, i.e. ansatz (4.11), as employed by Samanta *et al.* (2013), is too restrictive.

6. Time-dependent simulations

In this section, we present some time-dependent numerical simulations of the three-equation full and approximate models (4.2), (4.10), and (4.17), (4.16) and the no-slip model (4.17), (4.19) with outlet open boundary conditions and forcing at the inlet (open flow). Computations have been performed using finite differences and the method of lines, which can be easily employed in the case of evolution equations (Cellier & Ruyer-Quil 2019), for which the system of partial differential equations can be written as

$$U_t = F(U, U_x, U_{xx}, \dots), \tag{6.1}$$

where the indices refer to temporal or spatial derivatives; and U is the vector that contains the unknowns (in this particular case h, q and q_p). The spatial derivatives of our system (6.1) are first discretised and replaced by algebraic approximations using second-order central finite differences. As a consequence, (6.1) is transformed into an initial-value problem for the vector \tilde{U} of discrete unknowns on the chosen numerical grid:

$$\frac{d\tilde{U}}{dt} = \tilde{F}(\tilde{U}). \tag{6.2}$$

An in-house solver has been developed in Julia language in order to integrate (6.2). This solver uses the libraries ForwardDiff (Revels, Lubin & Papamarkou 2016) and DifferentialEquations (Rackauckas & Nie 2017). The ForwardDiff library implements forward-mode automatic differentiation algorithms and thus enables one to automatically and efficiently compute the Jacobian of the function \tilde{F} . As a result, changes of the model are easily implemented in the code. DifferentialEquations offers a wide range of schemes and algorithms for integration in time. We used a Crank–Nicolson scheme with adaptive time-stepping. This scheme is recommended for highly stiff problems and limits the numerical cost.

We present some simulations of a time-periodic wavy evolution generated by a regular forcing at the inlet:

$$q_i = I^{(i)}(1)[1 + A \sin(\omega t)]. \quad (6.3)$$

Outlet open boundary conditions are selected in order to reproduce experimental conditions. They consist of simple no-flux conditions at the domain outlet. Owing to the intrinsic convective nature of the studied phenomena, induced oscillations only affect a few nodes of the numerical domain at the outlet. Parameters are chosen to correspond to an experiment by Liu & Gollub (1994) with a dimensionless flow rate $R = q_N/\nu = 19.33$, a forcing frequency $f = 4.5$ Hz, angle $\theta = 6.4^\circ$, $\nu = 6.27 \times 10^{-6} \text{ m}^2 \text{ s}^{-1}$ and $Ka = 526$. We chose $\delta = 0.5$ and a moderate Darcy number $Da = 0.01$. The Reynolds number has been adjusted to $Re = 3R/[2(1 - \delta)] = 47.3$, which corresponds to a film on an impermeable substrate at $y = \tilde{\delta}$ (no-slip model). The no-slip model (4.17), (4.19) reproduces accurately the nonlinear multi-peaked wave evolution reported in the experiment (Ruyer-Quil & Manneville 2002). As it develops downstream, the flow remains periodic in time at the inlet forcing frequency. The initial exponential growth gives way to a multi-peaked wave with the growth of a secondary peak. A phase locking occurs and a modulated wave-train emerges. Our simulations with the full and approximate three-equation models (4.2), (4.10), and (4.17), (4.16) in the isotropic case $\xi = 1$ underline the effect of a thick porous layer on the wave evolution. In contrast to the remarkable agreement reported by Samanta *et al.* (2013) for a thin porous medium at $\delta = 0.1$, our simulations show that the flow in the porous medium significantly affects the wave evolution, mitigating the growth of a secondary peak, delaying the phase locking and the emergence of the modulated wave-train. The approximate and full models give results in close agreement.

In contrast to the no-slip model, the simulations performed with the full and approximate models at $\xi = 1000$ show the emergence of waves with a lower amplitude than for the isotropic case ($\xi = 1$). A quicker onset of the final modulated wave-train is observed. Spatial modulations of this wave-train are also weaker and quickly attenuated. This is clearly an effect of the viscous diffusion of the liquid momentum in the top Brinkman sublayer of the porous medium, which is promoted at low cross-stream permeabilities. In fact, we have checked that setting coefficients \tilde{J}_i^l , \tilde{K}_i^l , \tilde{L}_i^l and \tilde{M}_i^l to zero in the averaged momentum balance (4.10) for the liquid layer yields results in close agreement with the no-slip model at $\xi = 1000$. Similar results are obtained for the approximate model by dropping all terms proportional to ξ in (4.16a).

We next turn to a simulation of a solitary-like wave-train generated at a lower frequency $f = 1.5$ Hz, for which we discuss the effect of varying the Darcy number (see figure 13). At a moderate value of the Darcy number ($Da = 0.01$), raising anisotropy leads to a damping of the capillary ripples, which is consistent with the above observations for $f = 4.5$ Hz. However, lowering Da to $Da = 0.001$, anisotropy has an opposite effect, the amplitude of capillary ripples being raised as ξ is increased. These observations are consistent with our linear stability analysis (§ 3). Raising the cross-stream permeability affects the short capillary waves differently depending on the relative extension of the Darcy and Brinkman sublayer in the porous region. Results from the approximate models (not shown) are in close agreement with the full model. We note that $\xi Da^{3/2}$ equals 0.05 for $\xi = 1000$ and $Da = 0.001$, and 1.5 for $\xi = 1000$ and $Da = 0.01$, so that the contribution of cross-stream permeability to the viscous diffusion in the Brinkman top sublayer is weak in the former case and significant in the latter one. As expected, a close agreement is found between the solution to the no-slip model and the full three-equation model for $Da = 0.001$ and

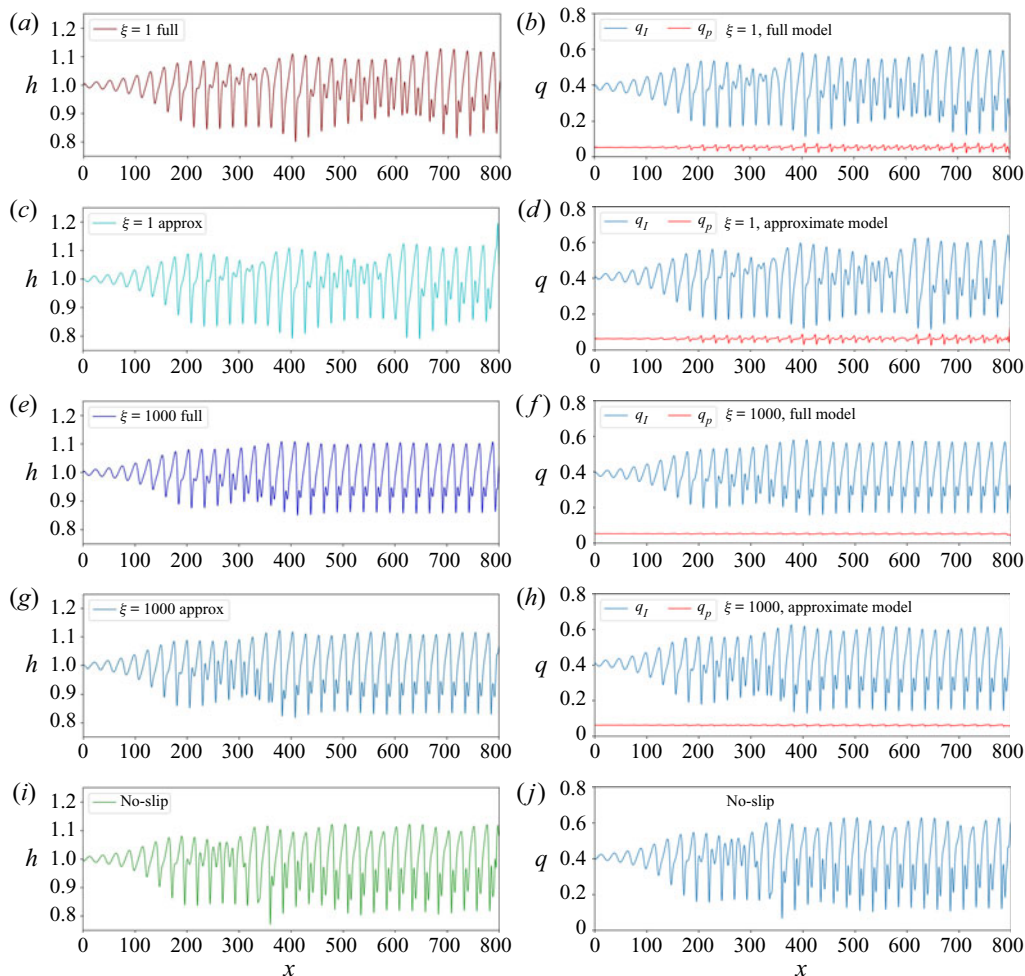


Figure 12. Simulations of a wave-train generated by a periodic inlet forcing using the no-slip model (4.17), (4.19), and the three-equation full and approximate models (4.2), (4.10), and (4.17), (4.16). Parameters correspond to an experiment conducted by Liu & Gollub (1994): $Re = 47.3, f = 4.5$ Hz, $\theta = 6.4^\circ$, $\nu = 6.27 \times 10^{-6} \text{ m}^2 \text{ s}^{-1}$ and $Ka = 526$.

$\xi = 1000$. This agreement results again from the efficient damping of the mass exchange between the liquid and porous layer, so that q_p is nearly constant at large values of ξ .

Finally, we present time-dependent simulations of the three-equation full model and the no-slip model in an extended domain. In order to simulate the natural evolution of the film as a response to ambient noise, we superimpose to a constant inlet flow rate a white-noise signal of weak amplitude, such that the inlet film flow rates $q_i(x = 0, t = 0) = I^{(i)} g(t)$, where $g(t)$ fluctuates in the interval $[0.9, 1.1]$. Figure 14 presents a snapshot of the film evolution at the end of the simulation. The typical coarsening dynamics of falling-film flows is clearly observable, as large-amplitude waves travel faster and capture the waves that precede them. The downstream dynamics of the flow is then organised by solitary waves in interaction (Chang & Demekhin 2002). In the isotropic case ($\xi = 1$), the flow rate q_p in the porous medium may rise to quite large values under the large-amplitude solitary waves, corresponding to roughly three times its value for the Nusselt uniform-film solution.

Falling film on an anisotropic porous medium

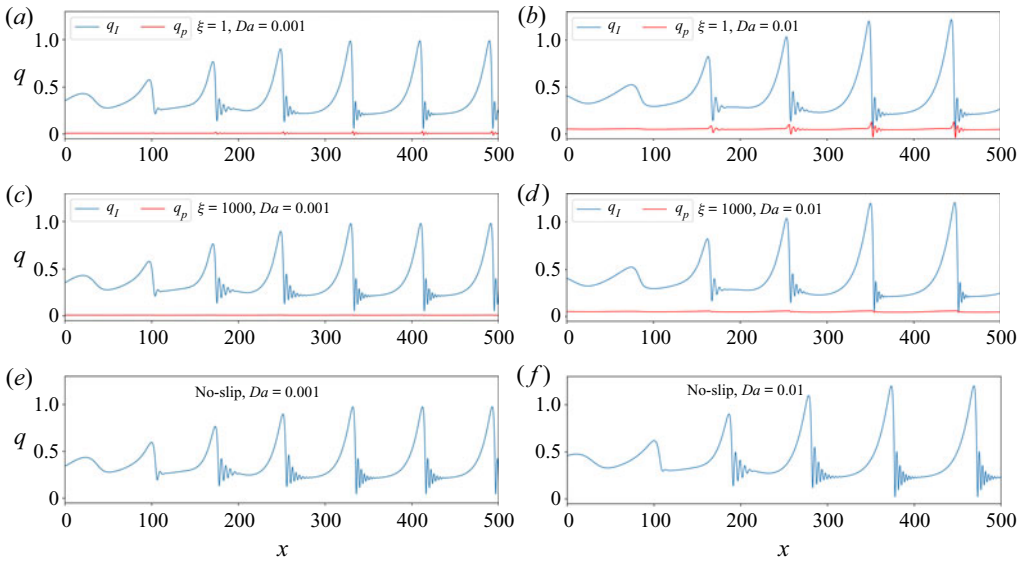


Figure 13. Simulations of a wave-train generated by a periodic inlet forcing using the three-equation full model (4.2), (4.10) and the no-slip model (4.17), (4.19) for different Darcy numbers. Parameters correspond to an experiment conducted by Liu & Gollub (1994): $Re = 47.3$, $f = 1.5$ Hz, $\theta = 6.4^\circ$, $\nu = 6.27 \times 10^{-6}$ m² s⁻¹ and $Ka = 526$. (a) $Da = 0.001$ and (b) $Da = 0.01$.

We thus conclude that the wavy dynamics of the film triggers an efficient exchange of mass between the porous and liquid media. Raising the cross-stream permeability ($\xi = 1000$) has a strong influence on the wave dynamics. Close to the inlet, nonlinear waves emerge more quickly out of the growth of random perturbations. Solitary waves observed at the outlet of the numerical domain have a lower amplitude.

A mitigation of the capillary ripples preceding the solitary waves is also evident, as well as the onset of bound states made of several linked waves and multi-peaked waves. All these phenomena arise from the influence of viscous diffusion on the velocity of the waves, an effect sometimes referred to as ‘viscous dispersion’ (Pradas, Tseluiko & Kalliadasis 2011). In contrast, the no-slip model (4.17), (4.19) presents interacting solitary waves whose shapes are similar to the isotropic case ($\xi = 1$), whereas the simulated wave evolution at the inlet is closer to the anisotropic one ($\xi = 1000$). This can be comprehended by considering that raising ξ attenuates the fluctuations of q_p and the no-slip model corresponds to $q_p = \text{const}$. Raising ξ also increases the viscous dispersion of the waves prompted by the Brinkman sublayer, an effect that is not accounted for by the no-slip model.

7. Summary and conclusions

The effects of anisotropy on the stability and nonlinear evolution of a falling film on an inclined plane have been investigated in the framework of a one-domain composite description of the entire liquid and porous domains introduced by Beckermann *et al.* (1988).

Extending the weighted residual modelling approach, a three-equation semi-analytical model (4.2), (4.10) has been derived by decoupling the flows in the porous and liquid regions. Two separate unknowns have thus been introduced to characterise the flow in these

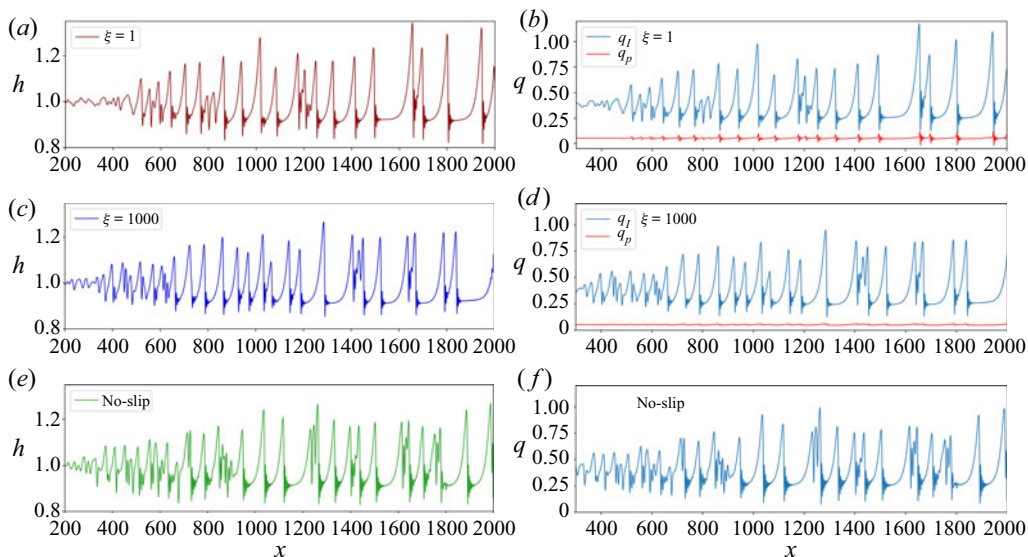


Figure 14. Simulations of the response of the film to noise at the inlet based on the three-equation full model (4.2), (4.10) and the no-slip model (4.17), (4.19). Panels (a) and (b) are snapshots of the free-surface elevation and flow rates in the liquid and porous region at the end of the simulation. Parameters are $Da = 0.01$, $\varepsilon_H = 0.78$, $\delta = 0.5$, $\Delta = 0.001$, $Ka = 769.8$ and $\theta = 4.6^\circ$.

two regions, i.e. the flow rates, q_l and q_p . The coefficients in the three-equation model have been numerically computed and tabulated. In the limit $Da \ll 1$, we have shown that this model can be simplified to (4.17), (4.16) using polynomial approximations of the velocity profile.

Orr–Sommerfeld stability analysis of the base flow has revealed a non-trivial dual effect of anisotropy on the film stability depending on the permeability of the porous medium. Raising ξ lowers the exchange of mass between the liquid and porous regions and therefore reduces the viscous damping of the film-height fluctuations in the Darcy sublayer at the core of the porous region. However, viscous diffusion of the film-height fluctuations is enhanced at the top Brinkman sublayer. The net balance of these two mechanisms depends on the relative size of the Brinkman and Darcy sublayers, therefore on the Darcy number.

In the isotropic case, when the thickness of the porous medium is relatively small (cf. figure 5), we observed the linear stability of the film on the porous substrate to be nearly equivalent to the stability of a film on an impermeable no-slip effective boundary located at $y = \delta - \delta_B$ (no-slip model). For a thicker porous layer, our computations show a weak amplification of the instability at the threshold at large permeabilities and an attenuation otherwise. This slight discrepancy on the instability threshold probably results from the significant differences observed for the velocity profiles in the porous region at large permeabilities (see figure 2). The attenuation of the instability further from threshold as compared to the no-slip model results from the viscous damping of the velocity fluctuations in the porous medium, which is allowed by the exchange of mass at the porous–liquid interface.

Our study of nonlinear waves has been based on the weighted residual three-equation models that we derived to account for the decoupling of the flows in the porous and liquid regions. This approach has been validated in the linear regime by comparison with the Orr–Sommerfeld analysis. The approximate model (4.17), (4.16) offers a welcome simplification of the full model (4.2), (4.10), which remains valid even at moderate values

of the Darcy number. It also enables us to propose a criterion, i.e. $\xi Da^{3/2} = O(1)$, above which the viscous diffusion in the Brinkman top sublayer becomes significant.

We have constructed nonlinear TW solutions by a continuation method and performed time-dependent simulations with open boundary conditions at the outlet (open flow). Raising ξ affects the wave shape and speed, modifying the connections of TW branches. TW solutions are close to the corresponding ones for the no-slip model (effective impermeable boundary at $y = \delta - \delta_B$) at low permeabilities. However, for the isotropic case $\xi = 1$, the intensity of the fluctuations of the flow rate q_p in the porous medium, and therefore the exchange of mass at the liquid–porous interface, is significant and impacts the amplitude of the capillary ripples.

Time-dependent simulations of the film response to a periodic forcing at the inlet have revealed a sharp effect of anisotropy on the time-periodic wave-trains. Raising ξ attenuates the fluctuations of q_p , thus limiting the mass exchange at the liquid–porous interface and mitigating the damping of film-height fluctuations in the Darcy sublayer. This mechanism amplifies the capillary ripples at low values of Da (cf. [figure 13](#)). However, damping of the capillary ripples is instead observed at larger values of Da when ξ is raised. This is explained by the increased efficiency of the viscous diffusion of the waves, as the intensity of the flow in the Brinkman sublayer is raised along with the permeability. Raising the anisotropy parameter ξ at moderate and large permeabilities also has a regularising effect on the inception of primary wave-trains generated by an inlet forcing (cf. [figure 12](#)), lowering the wave amplitude and damping the spatial modulations of the wave-trains. However, these effects on the stability and nonlinear dynamics of the liquid film are observed for fairly large values of the anisotropy parameter ($\xi = 10^3$). If very anisotropic porous media can be found in Nature, for instance, for faulty rocks where ξ can be as high as 10^4 (Evans, Forster & Goddard 1997; Farrell, Healy & Taylor 2014), it is difficult to think of a porous medium at the scale of a liquid film exhibiting such large anisotropy.

Finally, our time-dependent simulations of a noise-driven wavy film show that the fluctuations of the flow rate in the porous medium can be large due to the onset of large-amplitude solitary waves that dominate the dynamics of the film. Raising ξ at $Da = 0.01$ has a complex effect on the wave dynamics, modifying wave-to-wave interactions as a result of an enhanced dispersion of the waves prompted by the viscous diffusion in the Brinkman sublayer. We conclude that the influence of the flow in the porous layer on the film dynamics is much stronger than admitted in previous studies. The approximate three-equation model (4.17), (4.16) offers a reliable alternative to the more complex semi-analytical model (4.2), (4.10) and thus constitutes an interesting tool for later work.

Acknowledgements. The authors would like to thank the Department of Mathematics, IIT Madras, India, for providing all the facilities during the stay of S.M. during her doctoral mobility. We warmly thank A. Samanta for his help at an early stage of the project.

Funding. We acknowledge financial support from the Fraise project, grant ANR-16-CE06-0011 of the French National Research Agency (ANR) and from the project Optiwind through Horizon 2020/Clean Sky2 (call H2020-CS2-CFP06-2017-01) with Saint-Gobain. The stay of S.M. during her doctoral mobility was funded by a grant from Université Savoie Mont Blanc.

Declaration of interests. The authors report no conflict of interest.

Author ORCIDs.

-  Sanghasri Mukhopadhyay <https://orcid.org/0000-0001-5360-1190>;
-  Nicolas Cellier <https://orcid.org/0000-0002-3759-3546>;
-  Usha R <https://orcid.org/0000-0002-8026-6399>;

✉ Marx Chhay <https://orcid.org/0000-0003-4720-3713>;

✉ Christian Ruyer-Quil <https://orcid.org/0000-0002-7717-5015>.

Appendix A. Coefficients of the weighted residual model

The coefficients of the three-equation full model (4.2), (4.10) involve $f_i(y; H)$ and their derivatives with respect to H , $g_i = \partial_H f_i$, $a_i = \partial_{HH} f_i$, which satisfy

$$L g_i = -C'_{ij} \text{Id}_j, \quad g_i|_{y=0} = 0, \quad \partial_y g_i|_{y=H} = C_{il}, \quad \text{and} \quad \int_0^H \text{Id}_j g_i = -\delta_{jl} f_i(H; H) \tag{A1a}$$

and

$$L a_i = -C''_{ij} \text{Id}_j, \quad a_i|_{y=0} = 0, \quad \partial_y a_i|_{y=H} = 2C'_{il}, \quad \text{and} \quad \int_0^H \text{Id}_j a_i = -2\delta_{jl} g_i(H; H), \tag{A1b}$$

where $C'_{ij} = dC_{ij}/dH$ and $C''_{ij} = d^2 C_{ij}/dH^2$. The computation also involves the following functions:

$$l_i = \int_0^y f_i \, dy, \quad m_i = \int_0^y g_i \, dy, \quad b_i = \int_0^y a_i \, dy, \tag{A1c}$$

$$n_i = \int_H^y \frac{\partial_y f_i}{\varepsilon} \, dy, \quad o_i = \int_H^y \frac{\partial_y g_i}{\varepsilon} \, dy, \quad \beta_i = \int_H^y \frac{\partial_y a_i}{\varepsilon} \, dy, \tag{A1d}$$

$$r_i = \int_H^y \frac{l_i}{\kappa_x} \, dy, \quad s_i = \int_H^y \frac{m_i}{\kappa_x} \, dy, \quad \alpha_i = \int_H^y \frac{b_i}{\kappa_x} \, dy. \tag{A1e}$$

The expressions for the 54 coefficients are then as given below:

$$S_i^{(k)} = \frac{1}{H^2} \int_0^H f_i w_k \, dy, \tag{A2a}$$

$$F_{ij}^{(k)} = \frac{1}{H} \int_0^H \varepsilon^{-2} [\partial_y \varepsilon f_j l_i + (f_i f_j - \partial_y f_j l_i) \varepsilon - g_i \varepsilon^2] w_k \, dy, \tag{A2b}$$

$$G_{ij}^{(k)} = \int_0^H \varepsilon^{-2} [-\partial_y \varepsilon f_i m_j - \varepsilon (f_i g_j - \partial_y f_i m_j)] w_k \, dy, \tag{A2c}$$

$$J_i^{(k)} = 2g_i|_H w_k|_H + (2a_i|_H + C_{il}) \Upsilon_k + \int_0^H (a_i + \beta_i \varepsilon) w_k \, dy, \tag{A2d}$$

$$\tilde{J}_i^{(k)} = \int_0^H -\alpha_i \varepsilon w_k \, dy, \tag{A2e}$$

$$K_i^{(k)} = -2 \frac{1}{H} \left\{ f_i|_H w_k|_H + 2g_i|_H \Upsilon_k + \int_0^H (g_i + o_i \varepsilon) w_k \, dy \right\}, \tag{A2f}$$

Falling film on an anisotropic porous medium

$$\tilde{K}_i^{(k)} = \frac{2}{H} \int_0^H s_i \varepsilon w_k \, dy, \quad (\text{A2g})$$

$$L_i^{(k)} = \frac{1}{H} \left\{ (f_i|_H w_k|_H - 2g_i|_H \gamma_k) - \int_0^H (g_i + o_i \varepsilon) w_k \, dy \right\}, \quad (\text{A2h})$$

$$\tilde{L}_i^{(k)} = \frac{1}{H} \int_0^H s_i \varepsilon w_k \, dy, \quad (\text{A2i})$$

$$M_i^{(k)} = \frac{1}{H^2} \left\{ 2f_i|_H \gamma_k + w_k|_H + \int_0^H (f_i + n_i \varepsilon) w_k \, dy \right\}, \quad (\text{A2j})$$

$$\tilde{M}_i^{(k)} = -\frac{1}{H^2} \left\{ \int_0^H r_i \varepsilon w_k \, dy \right\}, \quad (\text{A2k})$$

$$\gamma_k = \int_0^H \varepsilon w_k \, dy, \quad (\text{A2l})$$

$$I^{(k)} = \gamma_k / H^3. \quad (\text{A2m})$$

These expressions must be contrasted with the corresponding ones for the two-equation model obtained by Samanta *et al.* (2013), who chose the one-function ansatz (4.11). We have carefully checked that, setting ξ to one and dropping the indices and suffices in (A2) yields the correct expressions for Samanta's model. However, they are written differently than in Samanta *et al.* (2013) due to a different – yet equivalent – choice (4.12a–d) for the definition of the test function f . We note that the base flow U_B satisfies

$$U_B = H^3 [I^{(l)}(H) f_l(y; H) + I^{(p)}(H) f_p(y; H)]. \quad (\text{A2n})$$

Since the reference scale for the velocity is the free-surface velocity of the base flow for the reference thickness $H = 1$, we have the relation

$$1 = I^{(l)}(1) f_l(1; 1) + I^{(p)}(1) f_p(1; 1). \quad (\text{A2o})$$

The linear stability analysis of the stationary solutions to the system (4.2) and (4.10) requires one to compute the variations with respect to H of the weights, which satisfy

$$L \partial_H w_i = 0, \quad \partial_H w_i|_{y=0} = 0, \quad \text{and} \quad \partial_H w_i|_{y=H} = \delta_{il} \frac{Re}{Fr^2}, \quad (\text{A2p})$$

so that $\partial_H w_p = 0$. We thus have

$$\frac{d(H^3 I^{(l)})}{dH} = w_l|_H + \int_0^H \varepsilon \partial_H w_l \, dy, \quad \text{and} \quad \frac{d(H^3 I^{(p)})}{dH} = w_p|_H. \quad (\text{A2q})$$

Appendix B. Approximation of the coefficients of the weighted residual model

We provide below the approximate expressions for the coefficients (A2) corresponding to the polynomial estimate of the velocity profile:

$$\begin{aligned}
 S_l^{(l)} &\approx \frac{4(H - \tilde{\delta})^2}{5(1 - \tilde{\delta})^2 H^2} + O(\delta_B^2), & S_p^{(l)} &\approx -\frac{2(H - \tilde{\delta})^3}{15(1 - \tilde{\delta})^2 \tilde{\delta} H^2} + O(\delta_B), \\
 F_{ll}^{(l)} &\approx \frac{68(H - \tilde{\delta})}{35(1 - \tilde{\delta})^2 H} + O(\delta_B^2), & F_{lp}^{(l)} &\approx -\frac{12(H - \tilde{\delta})^2}{35(1 - \tilde{\delta})^2 \tilde{\delta} H} + O(\delta_B), \\
 F_{pl}^{(l)} &\approx \frac{2(H - \tilde{\delta})(13\tilde{\delta} - 6H)}{35(1 - \tilde{\delta})^2 \tilde{\delta} H} + O(\delta_B), & F_{pp}^{(l)} &\approx \frac{(H - \tilde{\delta})^2(227\tilde{\delta} + 88H)}{420(1 - \tilde{\delta})^2 \tilde{\delta}^2 H} + O(\delta_B), \\
 G_{ll}^{(l)} &\approx \frac{36}{35(1 - \tilde{\delta})^2} + O(\delta_B^2), & G_{pp}^{(l)} &\approx -\frac{4(H - \tilde{\delta})^2}{35(1 - \tilde{\delta})^2 \tilde{\delta}^2} + O(\delta_B), \\
 G_{lp}^{(l)} = G_{pl}^{(l)} &\approx -\frac{1}{2} \left[\frac{4(H - \tilde{\delta})}{35(1 - \tilde{\delta})^2 \tilde{\delta}} \right] + O(\delta_B), & J_l^{(l)} &\approx \frac{16}{5(1 - \tilde{\delta})^2} + O(\delta_B^2), \\
 J_p^{(l)} &\approx \frac{2(H - \tilde{\delta})}{5(1 - \tilde{\delta})^2 \tilde{\delta}} + O(\delta_B), & \tilde{J}_l^{(l)} &\approx -\frac{6\delta_B^3}{5(1 - \tilde{\delta})^2 (H - \tilde{\delta})^3}, \\
 \tilde{J}_p^{(l)} &= \frac{2\delta_B^3}{5(1 - \tilde{\delta})^2 (H - \tilde{\delta})^2}, & K_l^{(l)} &\approx \frac{18(H - \tilde{\delta})}{5(1 - \tilde{\delta})^2 H} + O(\delta_B^2), \\
 K_p^{(l)} &\approx -\frac{2(H - \tilde{\delta})^2}{(1 - \tilde{\delta})^2 \tilde{\delta} H} + O(\delta_B), & \tilde{K}_l^{(l)} &\approx -\frac{4\delta_B^3}{5(1 - \tilde{\delta})^2 (H - \tilde{\delta})^2 H}, \\
 \tilde{K}_p^{(l)} &\approx \frac{2\delta_B^3}{5(1 - \tilde{\delta})^2 (H - \tilde{\delta})^2 \tilde{\delta} H}, & L_l^{(l)} &\approx \frac{24(H - \tilde{\delta})}{5(1 - \tilde{\delta})^2 H} + O(\delta_B^2), \\
 L_p^{(l)} &\approx -\frac{6(H - \tilde{\delta})^2}{5(1 - \tilde{\delta})^2 \tilde{\delta} H} + O(\delta_B), & \tilde{L}_l^{(l)} &\approx -\frac{2\delta_B^3}{5(1 - \tilde{\delta})^2 (H - \tilde{\delta})^2 H}, \\
 \tilde{L}_p^{(l)} &\approx \frac{\delta_B^3}{5(1 - \tilde{\delta})^2 (H - \tilde{\delta}) \tilde{\delta} H}, & M_l^{(l)} &\approx \frac{18(H - \tilde{\delta})^2}{5(1 - \tilde{\delta})^2 H^2} + O(\delta_B^2), \\
 M_p^{(l)} &\approx \frac{(8\tilde{\delta} - 3H)(H - \tilde{\delta})^2}{5(1 - \tilde{\delta})^2 \tilde{\delta} H^2} + O(\delta_B), & \tilde{M}_l^{(l)} &= -\frac{\delta_B^3}{5(1 - \tilde{\delta})^2 (H - \tilde{\delta}) H^2}, \\
 \tilde{M}_p^{(l)} &\approx \frac{\delta_B(H - \tilde{\delta})}{3H^2(1 - \tilde{\delta})^2} + O(\delta_B^2), & I^{(l)} &\approx \frac{2(H - \tilde{\delta})^3}{3(1 - \tilde{\delta})^2 H^3} + O(\delta_B^2), \\
 \frac{Re}{Fr^2} &\approx \frac{2}{(1 - \tilde{\delta})^2} + O(\delta_B^2),
 \end{aligned}$$

(B1a)

Falling film on an anisotropic porous medium

$$\begin{aligned}
 S_l^{(p)} &\approx \frac{2\delta_B^2}{(1-\tilde{\delta})^2 H^2} + O(\delta_B^4), & S_p^{(p)} &\approx \frac{2\delta_B^2}{(1-\tilde{\delta})^2 H^2} + O(\delta_B^3), \\
 F_{ll}^{(p)} &\approx \frac{24\delta_B^2}{5(1-\tilde{\delta})^2(H-\delta)H} + O(\delta_B^4), & F_{lp}^{(p)} &\approx F_{pl}^{(p)} \approx -\frac{4\delta_B^2}{5(1-\tilde{\delta})^2\tilde{\delta}H} + O(\delta_B^3), \\
 F_{pp}^{(p)} &\approx \frac{\delta_B^2(10\tilde{\delta} + 11\tilde{\delta}\varepsilon_H + 4H\varepsilon_H)}{5(1-\tilde{\delta})^2\tilde{\delta}^2\varepsilon_{HH}} + O(\delta_B^3), & G_{ll}^{(p)} &\approx \frac{12\delta_B^2}{5(1-\tilde{\delta})^2(H-\tilde{\delta})^2} + O(\delta_B^4), \\
 G_{pp}^{(p)} &\approx -\frac{2\delta_B^2}{5(1-\tilde{\delta})^2\tilde{\delta}^2} + O(\delta_B^3), & G_{lp}^{(p)} &= G_{pl}^{(p)} \approx O(\delta_B^3), \\
 J_l^{(p)} &\approx \frac{6\delta_B^2[2H + \tilde{\delta}(\varepsilon_H - 2)]}{(1-\tilde{\delta})^2(H-\tilde{\delta})^3} + O(\delta_B^4), & J_p^{(p)} &\approx -\frac{6\delta_B^2\tilde{\delta}^2}{(1-\tilde{\delta})^2(H-\tilde{\delta})^4} + O(\delta_B^3), \\
 \tilde{J}_l^{(p)} &\approx -\frac{6\tilde{\delta}^2\delta_B^2}{(1-\tilde{\delta})^2(H-\tilde{\delta})^4} + O(\delta_B^4), & \tilde{J}_p^{(p)} &\approx \frac{2\delta\delta_B^2}{(1-\tilde{\delta})^2(H-\tilde{\delta})^3} + O(\delta_B^3), \\
 K_l^{(p)} &\approx \frac{6\delta_B^2[2H + \tilde{\delta}(\varepsilon_H - 2)]}{(1-\tilde{\delta})^2(H-\tilde{\delta})^2H}, & K_p^{(p)} &\approx -\frac{2\delta_B^2}{(1-\tilde{\delta})^2\tilde{\delta}H} + O(\delta_B^3), \\
 \tilde{K}_l^{(p)} &\approx -\frac{4\delta_B^2\tilde{\delta}^2}{(1-\tilde{\delta})^2(H-\tilde{\delta})^3H}, & \tilde{K}_p^{(p)} &\approx \frac{2\delta_B^2\tilde{\delta}}{(1-\tilde{\delta})^2(H-\tilde{\delta})^2H} + O(\delta_B^3), \\
 L_l^{(p)} &\approx \frac{3\delta_B^2[4H + \tilde{\delta}(\varepsilon_H - 4)]}{(1-\tilde{\delta})^2(H-\tilde{\delta})^2H}, & L_p^{(p)} &\approx -\frac{3\delta_B^2}{(1-\tilde{\delta})^2\tilde{\delta}H} + O(\delta_B^3), \\
 \tilde{L}_l^{(p)} &\approx \frac{2\delta_B^2\tilde{\delta}^2}{(1-\delta)^2(H-\tilde{\delta})^3H} + O(\delta_B^4), & \tilde{L}_p^{(p)} &\approx -\frac{\delta_B^2\tilde{\delta}}{(1-\tilde{\delta})^2(H-\tilde{\delta})^2H} + O(\delta_B^3), \\
 M_l^{(p)} &\approx \frac{3\delta_B^2[3H + \tilde{\delta}(\varepsilon_H - 3)]}{(1-\tilde{\delta})^2(H-\tilde{\delta})H^2} + O(\delta_B^4), & M_p^{(p)} &\approx \frac{\delta_B^2[\tilde{\delta}(\varepsilon_H + 5) - H]}{(1-\delta)^2\tilde{\delta}H^2} + O(\delta_B^3), \\
 \tilde{M}_l^{(p)} &\approx -\frac{\delta_B^2\tilde{\delta}^2}{(1-\tilde{\delta})^2(H-\tilde{\delta})^2H^2} + O(\delta_B^4), & \tilde{M}_p^{(p)} &\approx \frac{2\tilde{\delta}^2}{3(1-\tilde{\delta})^2H^2} + O(\delta_B^4), \\
 I^{(p)} &\approx \frac{2\delta_B^2[H + \tilde{\delta}(\varepsilon_H - 1)]}{(1-\tilde{\delta})^2H^3} + O(\delta_B^4).
 \end{aligned}$$

(B1b)

REFERENCES

- AGUILAR-MADERA, C.G., VALDÉS-PARADA, F.J., GOYEAU, B. & OCHOA-TAPIA, J.A. 2011 Convective heat transfer in a channel partially filled with a porous medium. *Intl J. Therm. Sci.* **50** (8), 1355–1368.
- AMINI, Y., KARIMI-SABET, J., NASR ESFAHANY, M., HAGHSHENASFARD, M. & DASTBAZ, A. 2019 Experimental and numerical study of mass transfer efficiency in new wire gauze with high capacity structured packing. *Sep. Sci. Technol.* **54** (16), 2706–2717.
- ANGOT, P., GOYEAU, B. & OCHOA-TAPIA, J.A. 2017 Asymptotic modeling of transport phenomena at the interface between a fluid and a porous layer: jump conditions. *Phys. Rev. E* **95** (6), 063302.

- ARQUIS, E. & CALTAGIRONE, J.P. 1984 Sur les conditions hydrodynamiques au voisinage d'une interface milieu fluide-milieux poreux : application à la convection naturelle. *C. R. Acad. Sci. Paris (II)* **299**, 1–4.
- BEAVERS, G.S. & JOSEPH, D.D. 1967 Boundary conditions at a naturally permeable wall. *J. Fluid Mech.* **30** (1), 197–207.
- BEAVERS, G.S., SPARROW, E.M. & MAGNUSON, R.A. 1970 Experiments on coupled parallel flows in a channel and a bounding porous medium. *Trans. ASME J. Basic Engng* **92** (4), 843–848.
- BECKERMANN, C., VISKANTA, R. & RAMADHYANI, S. 1988 Natural convection in vertical enclosures containing simultaneously fluid and porous layers. *J. Fluid Mech.* **186**, 257–284.
- BRINKMAN, H.C. 1949 A calculation of the viscous force exerted by a flowing fluid on a dense swarm of particles. *Appl. Sci. Res.* **1** (1), 27.
- CAMPOREALE, C., MANTELLI, E. & MANES, C. 2013 Interplay among unstable modes in films over permeable walls. *J. Fluid Mech.* **719**, 527–550.
- CASTINEL, G. & COMBARNOUS, M. 1975 Convection naturelle dans une couche poreuse anisotrope. *Rev. Therm.* **168**, 937–947.
- CELLIER, N. & RUYER-QUIL, C. 2019 Scikit-finite-diff, a new tool for PDE solving. *J. Open Source Softw.* **4** (38), 1356.
- CHANDESRIS, M. & JAMET, D. 2006 Boundary conditions at a planar fluid–porous interface for a Poiseuille flow. *Intl J. Heat Mass Transfer* **49** (13), 2137–2150.
- CHANG, H.-C. & DEMEKHIN, E.A. 2002 *Complex Wave Dynamics on Thin Films*. Studies in Interface Science, vol. 14. Elsevier.
- CHANG, H.-C., DEMEKHIN, E.A. & KOPELEVITCH, D.I. 1993 Nonlinear evolution of waves on a vertically falling film. *J. Fluid Mech.* **250**, 433–480.
- CHANG, M.-H., CHEN, F. & STRAUGHAN, B. 2006 Instability of Poiseuille flow in a fluid overlying a porous layer. *J. Fluid Mech.* **564**, 287–303.
- CHEN, H. & WANG, X.-P. 2014 A one-domain approach for modeling and simulation of free fluid over a porous medium. *J. Comput. Phys.* **259**, 650–671.
- CRASTER, R.V. & MATAR, O.K. 2009 Dynamics and stability of thin liquid films. *Rev. Mod. Phys.* **81** (3), 1131–1198.
- DEEPU, P., KALLURKAR, S., ANAND, P. & BASU, S. 2016 Stability of a liquid film flowing down an inclined anisotropic and inhomogeneous porous layer: an analytical description. *J. Fluid Mech.* **807**, 135–154.
- DOEDEL, E.J., CHAMPNEYS, A.R., FAIRGRIEVE, T.F., KUZNETSOV, YU.A., SANDSTEDTE, B. & WANG, X. 2008 AUTO 97: continuation and bifurcation software for ordinary differential equations (with HomCont).
- DUARTE, S.I.P., FERRETTI, O.A. & LEMCOFF, N.O. 1984 A heterogeneous one-dimensional model for non-adiabatic fixed bed catalytic reactors. *Chem. Engng Sci.* **39** (6), 1025–1031.
- EPHERRE, J.F. 1975 Critère d'apparition de la convection naturelle dans une couche poreuse anisotrope. *Rev. Therm.* **168**, 949–950.
- EVANS, J.P., FORSTER, C.B. & GODDARD, J.V. 1997 Permeability of fault-related rocks, and implications for hydraulic structure of fault zones. *J. Struct. Geol.* **19** (11), 1393–1404.
- FARRELL, N.J.C., HEALY, D. & TAYLOR, C.W. 2014 Anisotropy of permeability in faulted porous sandstones. *J. Struct. Geol.* **63**, 50–67.
- FRISK, D.P. & DAVIS, E.J. 1972 The enhancement of heat transfer by waves in stratified gas-liquid flow. *Intl J. Heat Mass Transfer* **15** (8), 1537–1552.
- GOBIN, D., GOYEAU, B. & SONGBE, J.-P. 1998 Double diffusive natural convection in a composite fluid–porous layer. *Trans. ASME J. Heat Transfer* **120** (1), 234–242.
- HILL, A.A. & STRAUGHAN, B. 2008 Poiseuille flow in a fluid overlying a porous medium. *J. Fluid Mech.* **603**, 137–149.
- HIRATA, S.C., GOYEAU, B. & GOBIN, D. 2009 Stability of thermosolutal natural convection in superposed fluid and porous layers. *Transp. Porous Med.* **78** (3), 525–536.
- KALLIADASIS, S., RUYER-QUIL, C., SCHEID, B. & VELARDE, M.G. 2012 *Falling Liquid Films*. Applied Mathematical Sciences, vol. 176. Springer.
- LIU, J. & GOLLUB, J.P. 1994 Solitary wave dynamics of film flows. *Phys. Fluids* **6**, 1702–1712.
- LIU, J., SCHNEIDER, J.B. & GOLLUB, J.P. 1995 Three-dimensional instabilities of film flows. *Phys. Fluids* **7** (1), 55–67.
- LIU, R. & LIU, Q. 2009 Instabilities of a liquid film flowing down an inclined porous plane. *Phys. Rev. E* **80** (3), 036316.
- OCHOA-TAPIA, J.A. & WHITAKER, S. 1995 Momentum transfer at the boundary between a porous medium and a homogeneous fluid—I. Theoretical development. *Intl J. Heat Mass Transfer* **38** (14), 2635–2646.

Falling film on an anisotropic porous medium

- PASCAL, J.P. 1999 Linear stability of fluid flow down a porous inclined plane. *J. Phys. D: Appl. Phys.* **32** (4), 417–422.
- PRADAS, M., TSELUIKO, D. & KALLIADASIS, S. 2011 Rigorous coherent-structure theory for falling liquid films: viscous dispersion effects on bound-state formation and self-organization. *Phys. Fluids* **23** (4), 044104.
- RACKAUCKAS, C. & NIE, Q. 2017 Differentialequations.jl—a performant and feature-rich ecosystem for solving differential equations in julia. *J. Open Res. Softw.* **5** (1), 15.
- REVELS, J., LUBIN, M. & PAPAMARKOU, T. 2016 Forward-mode automatic differentiation in Julia. [arXiv:1607.07892](https://arxiv.org/abs/1607.07892) [cs.MS].
- RUYER-QUIL, C. & MANNEVILLE, P. 2002 Further accuracy and convergence results on the modeling of flows down inclined planes by weighted-residual approximations. *Phys. Fluids* **14** (1), 170–183.
- SADIQ, I.M.R. & USHA, R. 2008 Thin Newtonian film flow down a porous inclined plane: stability analysis. *Phys. Fluids* **20** (2), 022105.
- SAMANTA, A., GOYEAU, B. & RUYER-QUIL, C. 2013 A falling film on a porous medium. *J. Fluid Mech.* **716**, 414–444.
- SAMANTA, A., RUYER-QUIL, C. & GOYEAU, B. 2011 A falling film down a slippery inclined plane. *J. Fluid Mech.* **684**, 353–383.
- SCHEID, B., RUYER-QUIL, C., KALLIADASIS, S., VELARDE, M.G. & ZEYTOUNIAN, R.KH. 2005 Thermocapillary long waves in a liquid film flow. Part 2. Linear stability and nonlinear waves. *J. Fluid Mech.* **538**, 223–244.
- SHKADOV, V.YA. 1967 Wave flow regimes of a thin layer of viscous fluid subject to gravity. *Izv. Akad. Nauk SSSR Mekh. Zhidk. Gaza* **2**, 43–51, en. trans. in *Fluid Dyn.* **2** (Faraday Press, N.Y., 1970), 29–34.
- SHKADOV, V.YA. & SISOEV, G.M. 2004 Waves induced by instability in falling films of finite thickness. *Fluid Dyn. Res.* **35**, 357–389.
- SILVEIRA, A.C.P., TANGUY, G., PERRONE, Í.T., JEANTET, R., DUCEPT, F., DE CARVALHO, A.F. & SCHUCK, P. 2015 Flow regime assessment in falling film evaporators using residence time distribution functions. *J. Food Engng* **160**, 65–76.
- SISOEV, G.M. & SHKADOV, V.YA. 1999 A two-parameter manifold of wave solutions to an equation for a falling film of viscous fluid. *Dokl. Phys.* **44**, 454–459.
- SPARROW, E.M., BEAVERS, G.S., CHEN, T.S. & LLOYD, J.R. 1973 Breakdown of the laminar flow regime in permeable-walled ducts. *Trans. ASME J. Appl. Mech.* **40** (2), 337–342.
- TILTON, N. & CORTELEZZI, L. 2006 The destabilizing effects of wall permeability in channel flows: a linear stability analysis. *Phys. Fluids* **18** (5), 051702.
- TILTON, N. & CORTELEZZI, L. 2008 Linear stability analysis of pressure-driven flows in channels with porous walls. *J. Fluid Mech.* **604**, 411–445.
- VALDÉS-PARADA, F.J. & LASSEUX, D. 2021 A novel one-domain approach for modeling flow in a fluid–porous system including inertia and slip effects. *Phys. Fluids* **33** (2), 022106.
- DE WASCH, A.P. & FROMENT, G.F. 1972 Heat transfer in packed beds. *Chem. Engng Sci.* **27** (3), 567–576.
- YIH, C.-S. 1963 Stability of liquid flow down an inclined plane. *Phys. Fluids* **6** (3), 321.
- YOSHIMURA, P.N., NOSOKO, T. & NAGATA, T. 1996 Enhancement of mass transfer into a falling laminar liquid film by two-dimensional surface waves—some experimental observations and modeling. *Chem. Engng Sci.* **51** (8), 1231–1240.